Microwave Brightness Temperatures of Tilted Convective Systems

by

Ye Hong[1], Jeffrey L. Haferman[2], William S. Olson[3] and Christian D. Kummerow[4]

1 Caelum Research Corporation, Rockville, MD 20850

2 FNMOC, Monterey, CA 93943

3 JCET/University of Maryland Baltimore County, Baltimore, MD 21250

4 NASA/Goddard Space Flight Center, Greenbelt, MD 20771

Manuscript to be submitted to Journal of Applied Meteorology

November, 1998

Abstract

Aircraft and ground-based radar data from the Tropical Ocean and Global Atmosphere Coupled-Ocean Atmosphere Response Experiment (TOGA COARE) show that convective systems are not always vertical. Instead, many are tilted from vertical. Satellite passive microwave radiometers observe the atmosphere at a viewing angle. For example, the Special Sensor Microwave/Imager (SSM/I) on Defense Meteorological Satellite Program (DMSP) satellites and the Tropical Rainfall Measurement Mission (TRMM) Microwave Imager (TMI) on the TRMM satellite have an incident angle of about 50°. Thus, the brightness temperature measured from one direction of tilt may be different than that viewed from the opposite direction due to the different optical depth. This paper presents the investigation of passive microwave brightness temperatures of tilted convective systems.

To account for the effect of tilt, a 3-D backward Monte Carlo radiative transfer model has been applied to a simple tilted cloud model and a dynamically evolving cloud model to derive the brightness temperature. The radiative transfer results indicate that brightness temperature varies when the viewing angle changes because of the different optical depth. The tilt increases the displacements between high 19 GHz brightness temperature (Tb_{19}) due to liquid emission from lower level of cloud and the low 85 GHz brightness temperature (Tb_{85}) due to ice scattering from upper level of cloud. As the resolution degrades, the difference of brightness temperature due to the change of viewing angle decreases dramatically. The dislocation between Tb_{19} and Tb_{85}, however, remains prominent.

The successful launch and operation of the TRMM satellite provide us an opportunity to examine tilted convective systems using collocated radar and radiometer data. TMI observations of tilted systems indicate that dislocation between Tb_{19} and Tb_{85} can be as far as 100 km if there is a strong wind shear. Such dislocation not only poses a problem to rainfall retrieval algorithms

that use only scattering information, but also causes large uncertainty in rainfall retrieval from multichannel retrieval algorithms. This suggests that combined radar and radiometer data is needed to reduce the effect of tilt and to improve surface rainfall retrieval.

1. Introduction

Measurement of tropical rainfall is very important to understand the hydrological cycle and its role in the global climate system. Satellite observation of tropical rainfall is necessary due to the huge extent of oceans in the tropics. Comparing to visible/infrared observation, passive microwave observation provides better physical information for estimating surface rainfall because microwaves can penetrate clouds and interacts directly with hydrometeors at lower levels. Upwelling passive microwave brightness temperatures are determined by the surface and the vertical distributions of ice and liquid contents in clouds. At low microwave frequencies (< 37 GHz), the brightness temperature responds to emission from rain and cloud liquid and thus the observed brightness temperature increases over the radiometrically cold ocean. In contrast, at high frequencies (> 37 GHz), the brightness temperature responds to scattering from cloud ice and the observed brightness temperature decreases over both ocean and land backgrounds. Rainfall retrieval from satellite passive microwave brightness temperatures has been investigated by many researchers (Wilheit et al. 1977, Spencer et al. 1986, 1989, Kummerow et al. 1994, and Smith, et al. 1994).

Tropical precipitation generally occurs in the form of organized mesoscale convective systems (MCSs), which can be characterized by two distinguishable components: convective and stratiform (C/S) regions (see Zipser, 1977, Leary and Houze, 1979 and Houze, 1989 for the detailed descriptions of MCSs). Convective regions range from a few km to about 30 km in scale and have strong updrafts and downdrafts while stratiform regions may extend for hundreds of km and have relatively weak vertical air motion and light precipitation. Strong ice scattering has been observed by passive microwave radiometers to be associated with deep convection (Wilheit et al. 1982) due to the strong updrafts in convective regions. However, McGaughey, et al. (1996) has found significant ice scattering in stratiform precipitation regions. In such cases, wind shear causes the cloud top ice particles to shift horizontally away from heavy surface rainfall regions.

Therefore, if the significant vertical wind shear is present, 85 GHz brightness temperatures (Tb_{85}) that respond to cloud ice will be displaced from brightness temperature of 10 or 19 GHz channels (Tb_{10} or Tb_{19}) that respond primarily to surface rainfall and liquid hydrometeors in lower layers of clouds. Such tilted convective systems have been observed by aircraft radar and radiometer as well as ground-based radar during the Tropical Ocean and Global Atmosphere Coupled-Ocean Atmosphere Response Experiment (TOGA COARE). Figure 1 displays one case which was observed by the Airborne Rain Mapping Radar (ARMAR) and the Advanced Microwave Precipitation Radiometer (AMPR).

Satellite passive microwave radiometers, such as the Special Sensor Microwave/Imager (SSM/I) (Hollinger, et al. 1987) and the Tropical Rainfall Measurement Mission (TRMM) Microwave Imager (TMI) (Kummerow, et al. 1998), observe the atmosphere at a viewing angle. Thus, the brightness temperatures for a tilted system viewed from one direction of tilt may be different than those observed from the opposite direction due to different optical depth. The displacement between Tb_{85} and Tb_{19} and the viewing angle dependent brightness temperatures may result in errors of rainfall retrieval in a tilted system. Thus, investigation of microwave brightness temperatures of tilted convective systems is important for improving satellite rainfall retrieval.

In this paper, brightness temperatures of tilted systems at different channels and different viewing directions are investigated. Brightness temperatures are computed for a simple tilted cloud model and a cloud resolving model. To account for the effect of tilt, the 3D backward Monte Carlo transfer developed by Roberti (1994) is used and will be described in the section 2. Brightness temperatures of tilted systems calculated from cloud models will be presented and discussed in section 3. The successful launch and operation of the TRMM satellite provides us with an opportunity to examine tilted convective systems using collocated radar and radiometer

data. In section 4, satellite observations of tilted convective systems from Precipitation Radar (PR), TMI and SSM/I are presented. Conclusions and summary are given in section 5.

2. Radiative transfer model

Although 1-dimensional (1-D) plane parallel radiative transfer models are widely used in microwave spectral regions (Wilheit, 1977, Kummerow, 1993), 3-dimensional (3-D) radiative transfer models have been developed for horizontally and vertically finite clouds. Weinman and Davies (1978) first developed such a model, but they assumed vertical homogeneity. Kummerow and Weinman (1988) continued this study to include both liquid and ice layers and found that footprint-averaged brightness temperatures from finite clouds deviated considerably from the plane-parallel approximation. Haferman et al. (1993) used the discrete ordinates method to develop a 3-D radiative transfer model and reported that the nadir brightness temperatures from a finite cloud over land were lower than the nadir brightness temperature from a horizontally infinite cloud due to net leakage of radiation through the sidewalls of the cloud. Using a reverse Monte Carlo model, Petty (1994) described the reflected image of a finite cloud by the surface. Roberti et al. (1994) developed a 3-D backward Monte Carlo radiative transfer model and compared 1-D versus 3-D microwave radiative transfer. They observed that the brightness temperature pattern from 3-D microwave radiative transfer is shifted and enlarged when the viewing angle is nonzero.

The so-called 3-D effects, which is difference of brightness temperature over a finite cloud and a horizontally infinite cloud, can be attributed to geometric and physical problems (see Haferman, et al. 1996). Geometrically, nonzero view angles lead to a larger brightness temperature pattern than rainfall pattern and a horizontal shift between brightness temperature field and surface rain field. Physically, radiation from the side walls of a finite cloud and the reflected image of cloud

by the surface distorts the brightness temperature pattern from the surface rain field. The 3-D effects are also reported by Liu (1996) and Bauer et al. (1998).

To compute microwave brightness temperatures for a tilted system, a 3-D radiative transfer model must be used to account for the effect of the tilt. In this paper, we use the 3-D backward Monte Carlo radiative transfer model developed by Roberti et al. (1994). The backward Monte Carlo method tracks photons that are received by airborne or satellite-borne radiometers back to their sources through the medium, following probabilistic interaction laws which are sampled by the selection of numbers from a quasi-random sequence. The photons are either absorbed or scattered at an interaction point. If a photon is absorbed, it is considered as being emitted with the temperature at the point of absorption. When a photon is scattered, a new direction of travel is determined by the phase function, which is assumed to be a Henyey-Greenstein phase function having a given asymmetry factor. If a photon collides with the surface, scattering or absorption occurs depending on the surface emissivity and the random number. If a photon escapes from the upper boundary of the cloud, then it is considered as being emitted with the cosmic background temperature of 2.7 K.

Emission and absorption due to atmospheric gases (water vapor and oxygen) and hydrometeors, multiple scattering by hydrometeors, surface emission, and cosmic background radiation are all accounted for in this model. A more detailed description of the 3-D backward Monte Carlo model can be found in Roberti et al. (1994). The extinction and absorption coefficients of atmospheric gases (water vapor and oxygen) are computed using the formulas of Ulaby et al. (1981). Both liquid and ice are assumed to follow Marshall-Palmer drop size distributions. Radiative properties of atmospheric hydrometeors are computed using Mie theory.

3. Microwave brightness temperatures of tilted cloud models

To examine microwave brightness temperatures of tilted systems, the 3-D backward Monte Carlo radiative transfer model is applied to two cloud models. One is a simple finite cloud model and the other is the Goddard Cumulus Ensemble model (GCE), which is a cloud microphysical model developed primarily by Tao and Simpson (1993). Brightness temperatures at 19 and 85 GHz in horizontal polarization are computed at different viewing angles. For convenience, they will be referred as Tb_{19} and Tb_{85}. Results and discussion are given in this section.

a. Simple tilted cloud model

A simple finite cloud model was developed by Haferman et al. (1996) and is depicted in Fig.2a, where a 51 km x 51 km x 0.5 km thick cuboidal cloud is centered over a 5 km x 5 km x 4.5 km rain shaft and a 5 km x 5 km x 1 km ice layer is centered over the cloud layer. 5 km x 5 km is chosen because the TMI has such a resolution for 85 GHz. Following the Wilheit et al. (1977), the cloud model assumes that the relative humidity increases linearly from 80% at the surface to 100% at the freezing level of 5 km. The temperature of the atmosphere increases from 0 K at the freezing level to 305 K at surface with a lapse rate of 6.5 K/km, and the wind speed at the surface is set to 0 m/s. In order to account for the effect of tilt, we modified this model by assuming that the central rain shaft is tilted 45°. Figure 2b and 2c display side views of the vertical and tilted systems.

For the radiative transfer calculations, the cloud model uses 51 x 51 x 12 grid points with grid resolutions of 1 km horizontally and 0.5 km vertically respectively. The top boundary of the cloud is considered as cosmic background with a microwave brightness temperature equal to 2.7 K. The lower boundary is the surface which is assumed to be specular. For the tilt of 45°, the rain column will shift one grid point horizontally for every two vertical layers.

The 3-D backward Monte Carlo radiative transfer model is applied to the tilted cloud systems. Brightness temperatures for 19 and 85 GHz at the incident angle of 53° are computed for a rain rate of 20 mm/hr. Figure 3 presents the 19 GHz brightness temperature at the azimuth angles of 0° (solid line, looking from top right to bottom left) and 180° (dash line, looking from top left to bottom right). It can be seen that the brightness temperature pattern is larger than surface rain field. This is due to the tilt that results in an increase of the radiated area viewed by satellite, and also because radiation leaked from the sidewall of the cloud. To better understand these 3-D effects, the tilted rain column is overlaid on Fig. 3.

There are two differences for 19 GHz brightness temperatures when the tilted system is viewed from right and left (ψ = 0° and 180°). The first difference is that brightness temperature patterns have been shifted away from the surface rainfall fields in opposite directions. As discussed in Haferman et al. (1996), brightness temperatures of a central rain shaft observed by a satellite for an off-nadir angle (θ) is shifted horizontally from the surface rain field by a distance about $H\tan\theta$, where H is the mean height of the weighting function defined by Wu and Weinman (1984). The discussion of this geometric shift is beyond the scope of this paper. The second difference is that the Tb for ψ = 180° is less than the Tb for ψ = 0°. This is resulted from the different radiative transfer paths which one passes the cloud ice layer (ψ = 180°) while the other does not (ψ = 0°). The ice scattering creates a difference between the two viewing directions more than 20 K (see A_- and A_+ in Fig. 3).

Figure 4 shows the brightness temperatures of the tilted cloud for 85 GHz. The tilted rain column is also overlaid on the figure. Unlike the 19 GHz channel that responds to liquid hydrometers at lower layers in the cloud, the 85 GHz channel responds primarily to the ice on the top of a cloud. Thus, the 85 GHz brightness temperatures for azimuth angles of 0° and 180° depress at the same location where there is ice. However, the low Tb_{85} is shifted from the surface rainfall field due to tilt. Besides depression, the Tb_{85} is warmer than the background at

the satellite viewing sides (see A+ and A- in Fig. 4). This feature, resulting from the "reflected image", has been discovered by Olson (personal notes in 1989?) and reported by Petty (1994). It can be explained by the fact that the emission from liquid water at lower layers is reflected by the surface. This phenomena exists in all 85 GHz images shown later. For the azimuth angel ψ = 0°, the emission directly from liquid water at lower layers can also be observed by the satellite. The saw-like curve of Tb_{85} at A+ is probably due to the discontinuity of the tilted cloud layers. For the azimuth angel ψ = 180°, the increase of Tb_{85} at A- is caused by radiation from the side of the cloud layers and then reflected by the surface. The smoother change of Tb_{85} at B+ and B- in Fig. 4 is probably due to radiation leakage at the cloud edge.

Results from the simple tilted cloud model indicate that brightness temperature varies when azimuthal view angle changes. For 19 GHz, the difference could be 30K if ice is present when the surface rain field is viewed from the direction of tilt (ψ = 180°; see Tb at A- in Fig. 3) and viewed from the direction away from tilt (ψ = 0°; see Tb at A+ in Fig. 3). For 85 GHz, the depression of brightness temperatures viewed from both directions are very similar because the 85 responds to the ice on the top of the cloud. However, the higher Tb_{85} from the "reflected image" are located at different sides depending on azimuthal viewing angles.

b. GCE cloud model

In section 3a, we have tested a simple tilted cloud model. To better understand the effect of tilt, a more realistic dynamic cloud model, the GCE, is used in this section. The model assumes that liquid and ice are spherical. The distributions of rain, snow, and graupel (or hail) are taken to be inverse exponential with respect to the diameter (D) such that

$$N(D) = N_0 \exp(-\lambda D) \qquad (2)$$

where N(D) is the number of drops of diameter between D and D+dD per unit volume, N_0 is the intercept parameter and λ is the slope of the distribution given by:

$$\lambda = \left(\frac{\pi \rho_x N_0}{\rho q_x} \right)^{0.25} \tag{3}$$

The typical intercept parameters used in the GCE model for rain, snow and graupel are 0.08 cm^{-4}, 0.04 cm^{-4}, and 0.04 cm^{-4}, respectively. The density of rain, snow and graupel are 1 g cm^{-3}, 0.1 g cm^{-3} and 0.4 g cm^{-3} respectively. The cloud ice is monodisperse with a diameter of $2x10^{-3}$ cm and a density of 0.917 g cm^{-3}.

A tropical squall line from the development time of 60 minutes to 360 minutes has been simulated using the GCE model at a time interval of 60 minutes. The model domain is a 128 x 128 x 28 grid at a horizontal resolution of 3 km, and vertical resolutions of 0.5 km at the lower 20 layers and 1 km at the higher 8 layers. The tropical squall line was initialized from an environment observed on 22 Feb. 1993 during the TOGA COARE. Readers are referred to Tao et al (1993) for additional details. The integrated precipitating liquid and ice of the GCE model at the simulation time of 240 minutes is shown in Fig. 5a. Figure 5b shows the vertical profile of the precipitating liquid and ice at the cross line of AA'. It can be seen that the squall line is upshear-tilted.

The Monte Carlo radiative transfer model was applied to examine brightness temperature of the dynamical cloud model. Figures 6a and 6b present brightness temperatures for 19 GHz at azimuth angles of 0° and 180° respectively. One can see the apparent brightness temperature difference of the squall line for 19 GHz when viewed from the front (ψ = 0°) and from the rear (ψ = 180°). The strong emission of squall line in the leading edge is the combination of radiation directly from heavy rain and radiation from rain reflected by the surface (see Fig. 6a), while the emission from the leading edge of squall line has been attenuated by passing back through the

whole cloud system (see Fig 6b). Brightness temperatures for 85 GHz at azimuth angles of 0° and 180° are displayed in Fig. 6c and 6d respectively. Higher than background brightness temperatures can clearly be seen along the cloud boundary at the viewing sides.

Brightness temperatures along the cross line of AA' in Fig. 5a are displayed in Figs. 7 and 8. Figure 7a and 7b compare brightness temperatures at two azimuth angles for 19 GHz and 85 GHz respectively. Since the shift between the brightness temperature field observed by a satellite and the surface rain field due to the 3-D geometric effect may complicate the results caused by the tilt of a convective system, we have adjusted the locations of Tb_{19} to match the surface rain field and Tb_{85} to match the location of ice at the top of cloud. From Fig. 7a, we see that different optical paths result in a lower brightness temperatures for $\psi = 180°$. Due to radiation leaked from the side of the cloud, brightness temperatures along the cloud boundary is always higher at the viewing side than that viewed from the other side. Figure 7b shows that the locations for the strongest scattering of Tb_{85} at $\psi = 0°$ and $\psi = 180°$ differ by about 10 km (see B+ and B-). This may be the result of an atmosphere above the ice layer. Emission from the "reflected images" can be seen clearly at each viewing side (see A+ and A- in Fig. 7b).

Figures 8a and 8b compare 19 GHz and 85 GHz brightness temperatures for $\psi = 0°$ and $\psi = 180°$ respectively. As discussed previously, the 3-D radiative transfer model gives the brightness temperature at the top of atmosphere. Therefore, as long as there is a nonzero viewing angle, Tb_{19} actually responds to a different vertical profile of hydrometers than the Tb_{85} does. In other words, even in a vertically finite cloud system with liquid water in the lower cloud and ice in the upper cloud, 3-D computations of high Tb_{19} due to emission and low Tb_{85} due to scattering from the same vertical profile will be dislocated. The degree of dislocation depends on the thickness of cloud. This makes quantitative examination of displacement between Tb_{19} and Tb_{85} due to the tilt extremely difficult. But one thing we can conclude is that the tilt of a cloud will result in a large displacement between 19 and 85 GHz precipitation signatures. The scattering

features are also seen for 19 GHz data, especially for $\psi = 180°$ (see Fig. 8b).

c. Different satellite field of view (FOV)

Sections 3a and 3b give brightness temperatures at the resolutions of cloud models. However, what we are interested in is how brightness temperatures change in a satellite field of view (FOV). In this section, SSM/I and TMI data are considered.

The SSM/ has seven channels: 19.35 V&H, 22.235 V, 37 V&H, and 85.5 V&H GHz. The TMI also has the 19.35, 37 and 85.5 V&H channel pairs, plus two 10.7 GHz channels (V&H), and a 21.3 GHz water vapor absorption channel instead of the 22.235 GHz channel to avoid saturation in the tropics. TMI footprint dimensions range from about 40 km for the 10 GHz channels to 5 km for the 85.5 GHz channels. The SSM/I has horizontal resolutions from about 48 km for the 19.35 GHz channels to 13 km for the 85.5 GHz channels. Table 1 lists characteristics of the TMI and the SSM/I

The simulated brightness temperatures in a satellite FOV are computed by convolving the high resolution brightness temperature field with the antenna gain function. The antenna gain function has been discussed and used by Kummerow et al. (1996) and Olson et al (1996). Figures 9a and 9b display the 19 GHz brightness temperature from the GCE model at the TMI resolution (~20 km) for $\psi = 0°$ and $\psi = 180°$ respectively. Comparing Fig. 9a and 9b with Fig. 6a and 6b, one can see that the low resolution TMI data have smoothed features, such as the leading edge of squall line, compared to the high resolution images. For the SSM/I resolution, which is presented in Fig. 9c and 9d, the squall line is barely apparent when viewed from the rear of the system. Although the strong emission of the squall line is still visible at both TMI and SSM/I resolutions when viewed from the leading edge, the difference of brightness temperature across the segment AA' for azimuth angles of 0° and 180° is very small (see Fig. 11a and Fig. 13a).

Figures 10a - 10d present Tb_{85} from the GCE model at TMI and SSM/I resolutions for $\psi = 0°$ and $\psi = 180°$ respectively. Since the 85 GHz brightness temperature for TMI has a resolution of 5km, it almost retains the features at the GCE model's resolution (see Fig.10a and 10b). Although Tb_{85} from SSM/I show the smoothed GCE model features, the higher than background Tb_{85} due to emission from the side of the cloud are clearly displayed in Fig. 10c and 10d. Figures 11b and 13b present the Tb_{85} difference across the segment AA' for azimuth angles of 0° and 180° at TMI and SSM/I resolutions respectively. Figure 13b indicate that the Tb_{85} difference between azimuth angles of 0° and 180° for the SSM/I is small.

Figures 12a and 12b present the displacement between Tb_{19} and Tb_{85} of TMI for azimuth angles of 0° and 180° respectively. Figures 14a and 14b are the same as Figs. 12a and 12b but are for SSM/I. Note that the dislocation between high Tb_{19} due to emission and low Tb_{85} due to scattering is reduced as the resolution degrades.

The 3-D radiative transfer computation results for Tb_{19} and Tb_{85} indicate that the brightness temperature of a tilted system varies when viewed from two opposite directions of the tilt. The Tb_{85} will be displaced from Tb_{19} if wind shear exists. As the resolution degrades to satellite FOV, the difference of brightness temperatures viewed from two opposite directions of the tilt may be neglected. The dislocation between Tb_{19} and Tb_{85} signatures, however, depends on how strong the wind shear is. In other words, the displacement between Tb_{19} and Tb_{85} resulting from 3-D physical and geometric effects may be neglected for low resolutions of satellite data. But if wind shear causes ice particles in the upper cloud to shift more than several satellite footprints from the surface rainfall field, the displacement between Tb_{19} and Tb_{85} cannot be ignored (see next section). This poses a problem for those rain retrieval algorithms that use only scattering information.

4. Satellite microwave observations of tilted systems

Satellite observations of tilted convective systems have been noticed by some researchers. Using ground based radar data and infrared data from geostationary satellites, Zipser (1988) and Heymsfield and Fulton (1994) found that in propagating squall line systems, the coldest cloud tops dislocated from the leading edge to the extensive trailing anvil as the systems evolve. Such characteristics were also found during TOGA COARE (Rickenbach et al. 1998). However, those observations were limited to locations where there were ground based radars or aircraft field experiments. The success of the TRMM project has provided us an opportunity to examine the tilted systems globally and frequently, because TRMM carries both the high resolution microwave imager, TMI, and the first space-borne Precipitation Radar (PR). The PR is a cross-scanning 13.8 GHz radar which has a swath width of about 220 km, about one-third of TMI swath width. It can provide the 3-D distribution of rainfall intensity at a horizontal resolution of about 4.4 km and vertical resolution of about 250m. The vertical rainfall profile from PR data can be used to detect the tilted system. TMI observations of tilted systems at 19 GHz and 85 GHz are examined in this section. For comparison, collocated and coincident SSM/I observations are also presented.

The SSM/I data we used can be obtained from the Global Hydrology Resource Center at NASA/MSFC (http://ghrc.msfc.nasa.gov). TRMM data are available from NASA/Goddard DAAC (http://daac.gsfc.nasa.gov).

a. Case of January, 05, 1998

A convective system from 5 January 1998 is depicted in Fig. 15. Figure 15a displays the near surface PR reflectivity and Figure 15b shows the cross section of reflectivity along line AA'. Figure 15b indicates that the maximum surface rainfall occurs around 30°S and 132.5°W, while a large part of ice particles aloft occur over the region west of 133°W. Existence of a bright band

from 133°W to 133.75°W suggests that the rainfall is strtiform in nature in this region. Thus, ice particles do not locate above the convective region, but in the stratiform region. Some were even in the precipitation-free region.

Brightness temperatures for 19 and 85 GHz (horizontal polarization) from TMI are presented in Figs. 16a and 16b respectively. Note that the warm Tb_{19} in Fig. 16b corresponds to the high surface reflectivity shown in Fig. 16a. Fig. 16c shows the Tb_{19h} and Tb_{85h} along the cross line AA'. Notice the lowest Tb_{85} along AA' , which responds to the strongest ice scattering, is about 1° west away from the highest Tb_{19}.

Figures 17 a-c are the same as those in Figures 16 a-c but for SSM/I observation of the case. Although the brightness temperatures vary more smoothly due to the degradation of spatial resolution, the shift between the maximum Tb_{19} and minimum Tb_{85} are still apparent in Fig. 17c.

b. Case of August 25, 1998

Figures 18 illustrates the case for the Hurricane Bonnie on 25 August 1998. The near surface PR reflectivity and the vertical cross section along line AA' (from 29°N and 75°W to 32°N and 72°W) are shown on Fig. 18a and 18b respectively. A strong convective core appears around 29.75°N and 74.25°W, and PR data show apparent attenuation below the height of 3 km. However, a large amount of ice particles have moved into the region center over 30.25°N and 73.75°W.

The brightness temperatures for 19 and 85 GHz channels from both TMI and SSMI are presented in Fig. 19 and Fig. 20 respectively. Comparing to Fig. 18, one can see that high resolution PR data display a very narrow (about 10 km) rainfall band pattern while TMI data can not distinguish such narrow band. Nevertheless, the displacements between 19 GHz and 85 GHz brightness temperatures along the line AA' can be seen in both TMI (Fig. 19c) and SSM/I

data (Fig. 20c). Note that near the longitude 74°W, the cold Tb_{85} occur along the latitude 30°N while the warm Tb_{19} appear along 29.75°N.

Passive microwave observations of the above two cases confirm the results derived from model simulations, and show that the dislocation between heavy surface rainfall region and ice particles aloft can be as large as 100 km if there is significant wind shear associated with convective systems. TMI simulations yield results consistent with observation. Although model simulations of SSM/I in section 3 do not show a large displacement between SSM/I Tb_{19} and Tb_{85}, the satellite observation suggest that even for low resolution SSM/I data, such displacement can be appreciable. The displacement of Tb_{85} from surface rainfall is a potential problem for single channel 85 GHz surface rainfall retrieval algorithms and also potentially casts large retrieval uncertainty to multichannel retrieval algorithms. Such retrieval uncertainty has been found in the TRMM operational algorithm 2A12 results for the above two cases (not shown). For TRMM operational algorithms, readers are referred to Kummerow et al. (1999).

5. Summary

Passive microwave brightness temperatures at 19 and 85 GHz of tilted convective systems have been examined using data computed from cloud models and measured from satellite radiometers. To account for the effect of tilt, a 3-D backward Monte Carlo radiative transfer model has been applied to a simple tilted cloud model and to the GCE model to derive brightness temperatures. Results from the simple tilted cloud model indicate that brightness temperatures vary when azimuthal viewing angle changes. The difference of 19 GHz brightness temperatures over the surface rain field is caused by differing optical thicknesses from two opposite viewing directions. For 85 GHz, the depression of brightness temperatures viewed from both directions are very similar because the 85 GHz channel responds primarily to ice on the top of the cloud. However,

the higher than background Tb_{85} due to emission from the side of the cloud are located at different sides depending on azimuthal viewing angles.

Results from the GCE model show similar features. When viewed from the leading edge of a squall line, strong emission is apparent due to the radiation leakage from the side of the cloud. Viewed from the rear, however, the emission from the heavy surface rainfall field is reflected by the ice on the top of cloud so that Tb_{19} is depressed. Due to the existence of atmosphere above the ice layer, the 85 GHz depression is shifted about 5 km when viewed from opposite directions. Another finding of this study is that warm Tb_{85}, due to emission from the side of cloud, exists along the cloud boundary at the viewing side. This phenomena cannot be reproduced using a plane-parallel radiative transfer model.

Because Tb_{19} responds to the low level of clouds and Tb_{85} responds to the upper level of clouds, the 3-D radiative transfer model-derived Tb_{19} will be displaced from Tb_{85} if there is a non-zero zenith viewing angle. This is true even for a vertical cloud system. But the displacement in vertical systems due to the 3-D geometric and physical effects may be ignored for low resolution satellite data. Results from section 3c suggest that such displacements are reduced dramatically as the resolution degrades.

The existence of significant wind shear, however, will increase such displacements. Satellite observations of tilted systems indicate that dislocation between Tb_{19} and Tb_{85} cannot be neglected if there is strong wind shear. Measurements from TMI and SSM/I show that Tb_{85} is displaced from Tb_{19} by as much 100 km in the Hurricane Bonnie case. Such dislocation adds to uncertainty in rainfall retrieval.

The investigation of brightness temperatures in tilted systems suggests that care must be taken when scattering information from 85 GHz data is used as an indicator of surface rainfall or other

index, such as separation of convective and stratiform regions (Anagnostou and Kummerow, 1996, Hong, et al. 1999). This is particularly true for the higher resolution TMI 85 GHz data. Using TMI data only, it may be difficult to detect the direction of tilt and remove the effect of tilt in surface rainfall retrieval. Combined with high resolution PR data, however, the effect of tilt can be reduced, and the surface rainfall retrieval from satellite data will be improved.

Acknowledgments: We would like to thank Drs. Dave Short and Tom Rickenbach for their helpful discussion. This work was funded by the TRMM science program.

References

Anagnostou, E. N. and C. Kummerow, 1996: Stratiform/Convective Classification of Rainfall using SSM/I 85 GHz Brightness Temperature Observations, *J. Atmos. and Ocean Tech.*, **14,** 570 - 575.

Bauer, P., L. Schanz, R. Bennartz and P. Schlussel, 1998: Outlook for combined TMI-VIRS algorithms for TRMM: Lessons from the PIP and AIP projects, *J. Atmos. Sci.*, **55,** 1714-1729

Haferman, J. L., E.N.Anagnostou, D.Tsintikidis, W.F.Krajewski and T.F.Smith, 1996, Physically based satellite retrieval of precipitation using a 3D passive microwave radiative transfer model, *J. Atmos. and Oceanic Techno.*, **13,** 832 - 850.

Heymsfield, G. M., and R. Fulton, 1994: Passive microwave and infrared structure of mesoscale convective systems. *Meteor. Atmos. Phys.*, **54,** 123-139.

Houze, R. A. Jr., 1989: Observed structure of mesoscale convective systems and implications for large-scale heating. *Quart. J. Roy. Meteor. Soc.*, **115,** 425-461.

—, 1993: *Cloud Dynamics*. Academic Press, San Diego, 573pp.

Kummerow, C. , 1993: On the accuracy of the Eddington approximation for radiative transfer in the microwave frequencies. *J. Geophys. Res.*, **98,** 2757-2765.

—, and L. Giglio, 1994a: A passive microwave technique for estimating rainfall and vertical structure information from space. Part I: Algorithm Description. *J. Appl. Meteor.*, **33,** 3-18.

—, and L. Giglio, 1994b: A passive microwave technique for estimating rainfall and vertical structure information from space. Part II: Applications to SSM/I data. *J. Appl. Meteor.*, **33,** 19-33.

—, and coauthors, 1999: A passive microwave technique for estimating rainfall and vertical structure information from space. Part I: Algorithm Description. *J. Appl. Meteor.*, **33,** 3-18.

Leary, C. A., and R. A. Houze, Jr., 1979: The structure and evolution of convection in a tropical cloud cluster. *J. Atmos. Sci.*, **36,** 437-457

Liu, Q., C, Simmer, and E. Ruprecht, 1996, Three-dimensional radiative transfer effects of clouds in the microwave spectral range, *J. Geophys. Res.*, **101,** 4289-4298.

McGaughey, G., E. J. Zipser, R. W. Spencer and R. E. Hood, 1996: High resolution passive microwave observations of convective systems over the tropical pacific ocean. *J. Appl. Meteor.* **35,** 1921-1947

Petty, G.W., 1994, Physical retrievals of over-ocean rain rate from multichannel microwave imagery. Part I: Theoretical characteristics of normalized polarization and scattering indices, *Meteor. Atmos. Phys.*, **54,** 79-99.

Rickenbach, T. M., D. A. Short and O. W. Thiele, 1997, Propagation characteristics of tropical convective systems from radar and infrated satellite images. *Preprints, 28th Conference on Radar Meteorology,* Sept. 7-12, Austin, TX. Amer. Meteor. Soc., 596 - 597.

Roberti, L., J .L. Haferman and C. Kummerow, 1994, Microwave radiative transfer through horizontally inhomogeneous precipitating clouds. *J. Geophys. Res.*, **99,** 16707 - 16718.

Smith, E. A., A. Mugnai, H. J. Cooper, G. J. Tripoli, and X. Xiang, 1992: Foundations for statistical physical precipitation retrieval from passive microwave satellite measurements. Part I: Brightness temperature properties of a time-dependent cloud radiation model. *J. Appl. Meteor.,* **31,** 506-531.

Spencer, R. W., R. E. Hood, F. J. LaFontaine, E. A. Smith, J. Galliano, and E. Lobl, 1994: High resolution imaging of rain systems with the Advanced Microwave Precipitation Radiometer. *J. Atmos. Oceanic Technol.* **11,** 849 - 857.

Tao, W.-K., and J., Simpson, 1989: Modeling study of a tropical squall-type convective line. *J. Atmos. Sci.*, **46,** 172-202.

—, —, 1993a: Goddard Cumulus Ensemble model, Part I: Model description. *TAO,* **4,** 35-72

—, —, C.-H. Sui, S. Lang, J., Simpson, and R. Adler, 1993b: Retrieval algorithms for estimating the vertical profiles of latent heat release: their applications for TRMM. *J. Meteor. Soc. Japan,* **71,** 685-700

Ulaby, F.T., R.K.Moore, and A.K. Fung, 1981, Microwave Remote Sensing, Active and Passive.

Vol. I. Microwave Remote Sensing: Fundamentals and Radiometry, Artech House, 456 pp, 1981

Wilheit, T. T., A. T. C. Chang, M. S. V. Rao, E. B. Rodgers and J. S. Theon, 1977: A satellite technique for quantitatively mapping rainfall rates over the oceans. *J. Appl. Meteor.*, **16,** 551-560.

—, —, J. L. King, E. B. Rodgers, R. A. Nieman, B. M. Krupp, A. S. Milman, J. S. Stratigos, and H. Siddalingaiah, 1982: Microwave radiometric observations near 19.35, 92, and 183 GHz of precipitation in tropical storm Cora. *J. Appl. Meteor.*, **21,** 1137-1145.

Zipser, E. J., 1977: Mesoscale and convective-scale downdrafts as distinct components of squall-line circulation. *Mon. Wea. Rev.*, **105,** 1568- 1589.

Figure Captions

Figure 1: A tilted convective system observed during TOGA COARE. a) radar reflectivities from ARMAR; b) brightness temperatures from AMPR for 10, 19, 37 and 85 GHz.

Figure 2: A simple tilted cloud model. a) overview of vertical system; b) sideview of the vertical rain shaft; and c) sideview of tilted rain shaft.

Figure 3: 19 GHz brightness temperature of the simple tilted cloud model at the azimuth angles of 0° (solid line, looking from top right to bottom left) and 180° (dash line, looking from top left to bottom right). The tilted rain shaft is overlaid.

Figure 4: Same as the Fig. 3 except for 85 GHz.

Figure 5: The GCE cloud model at the simulation time of 240 minutes. a) integrated precipitating liquid and ice; b) vertical profile of the precipitating liquid and ice at the cross line of AA'.

Figure 6: Brightness temperatures from the GCE cloud model. a) 19 GHz, azimuth angle = 0° (looking from right side to left); b) 19 GHz, azimuth angle = 180° (looking from left side to right); c) 85 GHz, azimuth angle = 0°; and d) 85 GHz, azimuth angle = 180°.

Figure 7: Comparison of brightness temperatures along the cross line of AA' at different azimuth angles. a) 19 GHz for azimuth angle = 0° (solid line) and azimuth angle = 180° (dash line); b) 85 GHz for azimuth angle = 0° (solid line) azimuth angle = 180° (dash line).

Figure 8: Comparison of brightness temperatures along the cross line of AA' at different channels. a) azimuth angle = 0° for 19 GHz (solid line) and 85 GHz (dash line); b) azimuth angle

= 180° for 19 GHz (solid line) and 85 GHz (dash line).

Figure 9: 19 GHz brightness temperatures of the GCE model at satellite radiometer resolution. a) TMI, azimuth angle = 0°; b) TMI azimuth angle = 180°; c) SSMI, azimuth angle = 0°; and d) SSMI azimuth angle = 180°

Figure 10: Same as the Fig. 9 except for the 85 GHz.

Figure 11: Same as the Fig. 7 except at TMI resolution

Figure 12: Same as the Fig. 8 except at TM/I resolution

Figure 13: Same as the Fig. 7 except at SSMI resolution

Figure 14: Same as the Fig. 8 except at SSM/I resolution

Figure 15: Radar reflectivity from PR for the January 5 1998 case. a) near surface reflectivity; and b) cross section of reflectivity along line AA'.

Figure 16 TMI observations of the January 5 1998 case. a) 85 GHz; b) 19 GHz; and c) Tb_{85} and Tb_{19} along the cross line of AA'. Lines on a) and b) are PR swath.

Figure 17 Same as the Fig. 16 except for SSM/I observations.

Figure 18 Radar reflectivity from PR for the Hurricane Bonnie case on Aug. 25, 1998. a) near surface reflectivity; and b) cross section of reflectivity along line AA'.

Figure 19 TMI observations of the Hurricane Bonnie case on Aug. 25, 1998. a) 85 GHz; b) 19 GHz; and c) Tb_{85} and Tb_{19} along the cross line of AA'.

Figure 20 Same as the Fig. 19 except for SSM/I observations.

Table 1. Characteristics of the TMI and the SSM/I

Instrument	Frequency (GHz)	Spatial Resolution (km)	Polarization (H, V)
SSM/I	19.35	69 x 43	H, V
	22.235	50 x 40	V
	37	37 x 29	H, V
	85.5	15 x 13	H, V
TMI	10.7	63 x 37	H, V
	19.35	30 x 18	H, V
	21.3	23 x 18	V
	37	16 x 9	H, V
	85.5	7 x 5	H, V

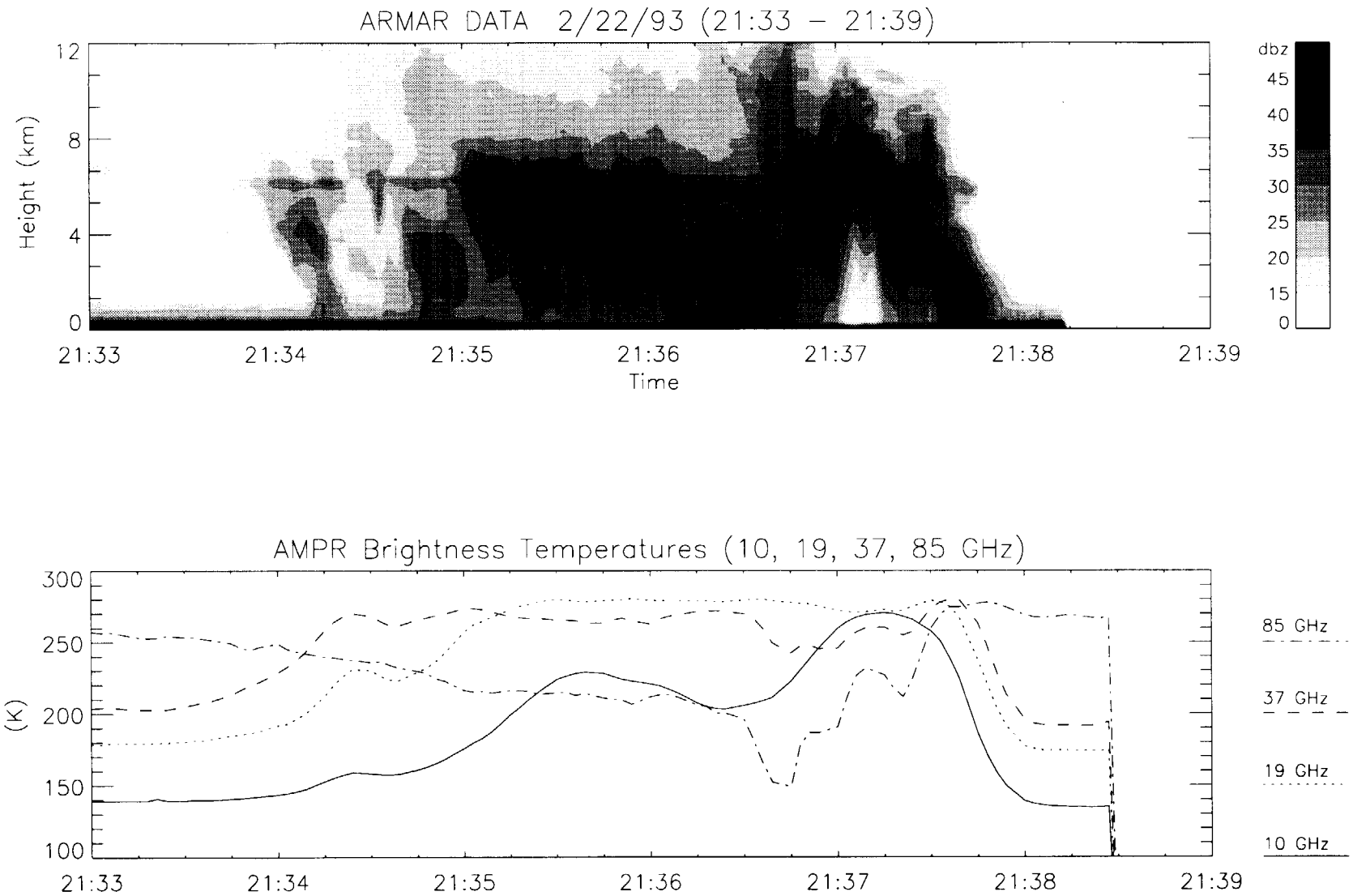
ARMAR DATA 2/22/93 (21:33 – 21:39)
Height (km)
12
8
4
0
21:33
21:34
21:35
21:36
21:37
21:38
21:39
Time
dbz
45
40
35
30
25
20
15
0
AMPR Brightness Temperatures (10, 19, 37, 85 GHz)
(K)
300
250
200
150
100
21:33
21:34
21:35
21:36
21:37
21:38
21:39
85 GHz
37 GHz
19 GHz
10 GHz

Fig. 1

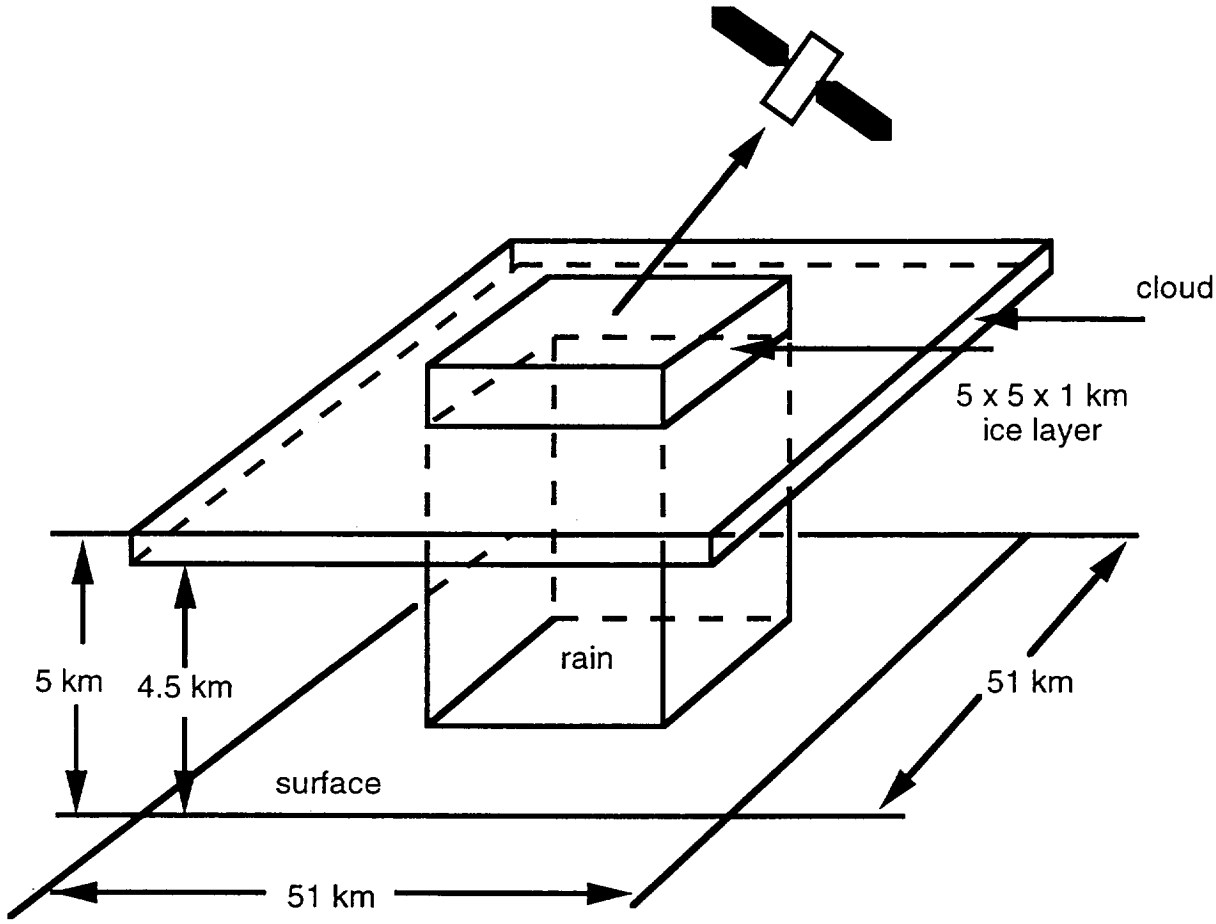

a

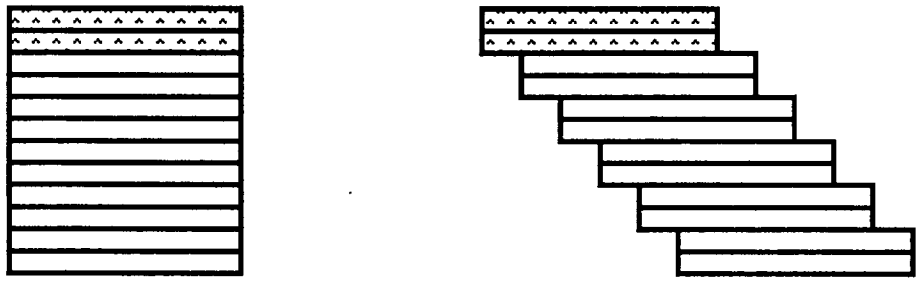

b

c

Fig. 2

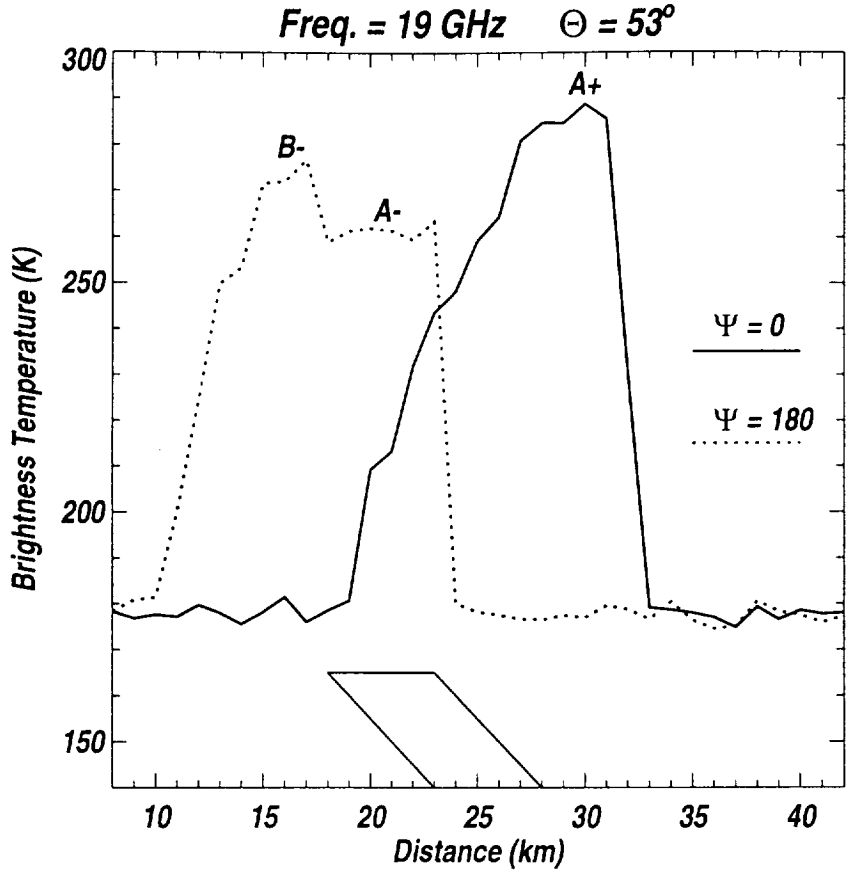
Freq. = 19 GHz Θ = 53°
300
250
200
150
Brightness Temperature (K)
A+
B-
A-
Ψ = 0
Ψ = 180
10
15
20
25
30
35
40
Distance (km)

Fig. 3

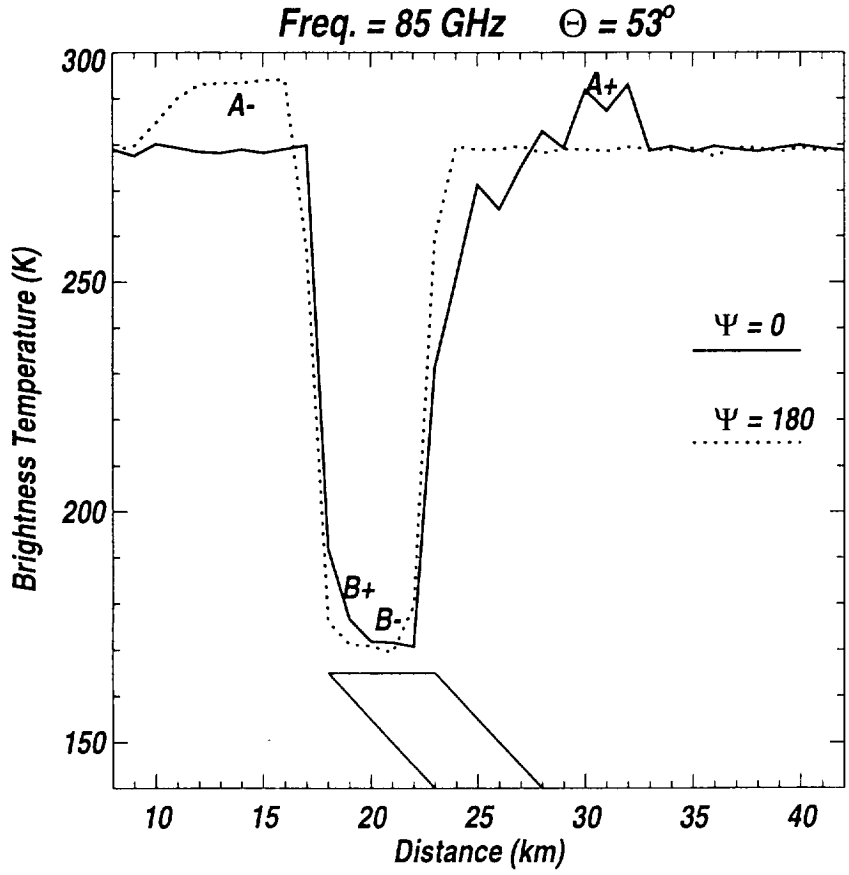
Freq. = 85 GHz Θ = 53°
300
250
200
150
Brightness Temperature (K)
A-
A+
B+
B-
Ψ = 0
Ψ = 180
10
15
20
25
30
35
40
Distance (km)

Fig. 4

TOGA COARE GCE model (240 min.)

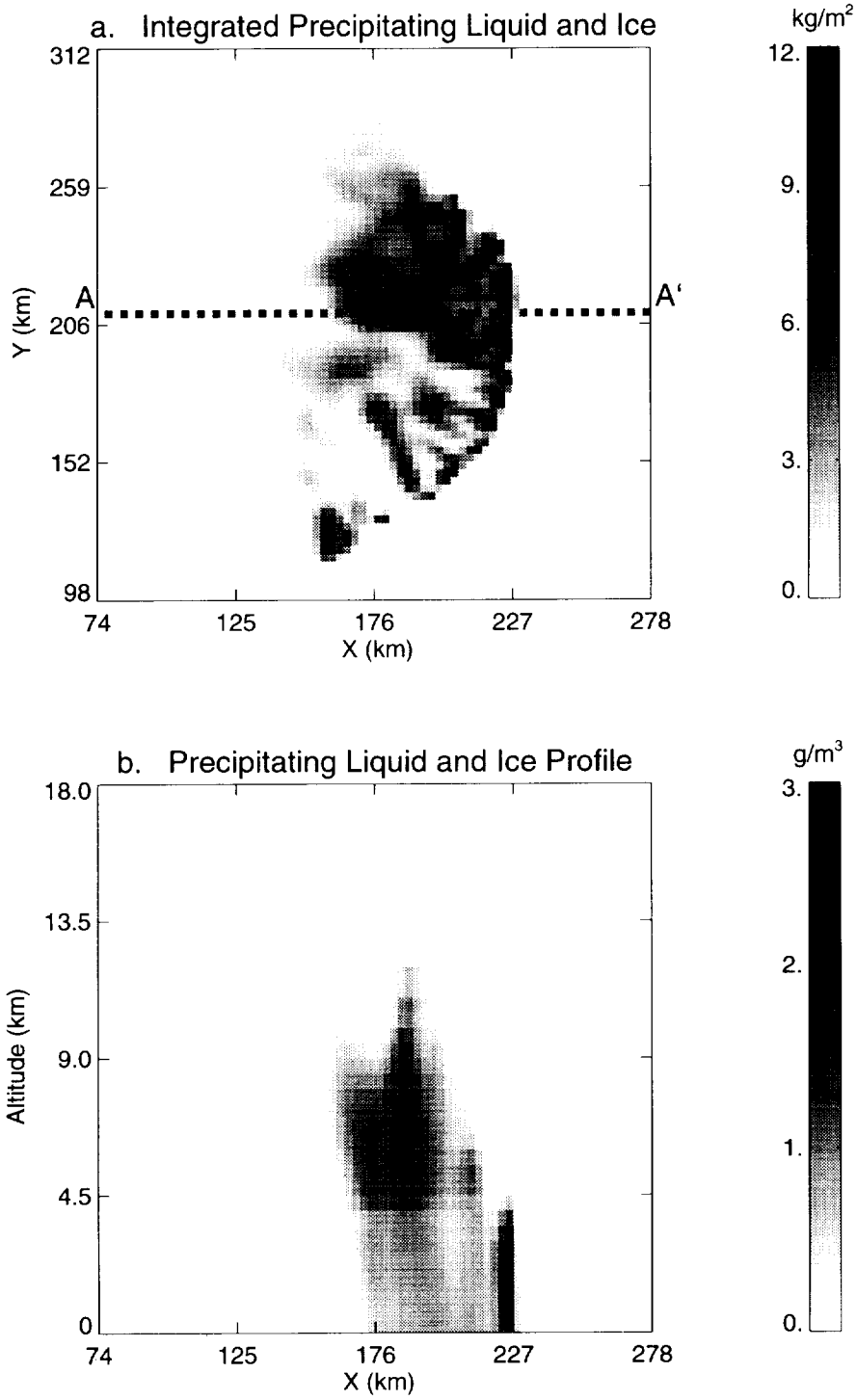

Fig. 5

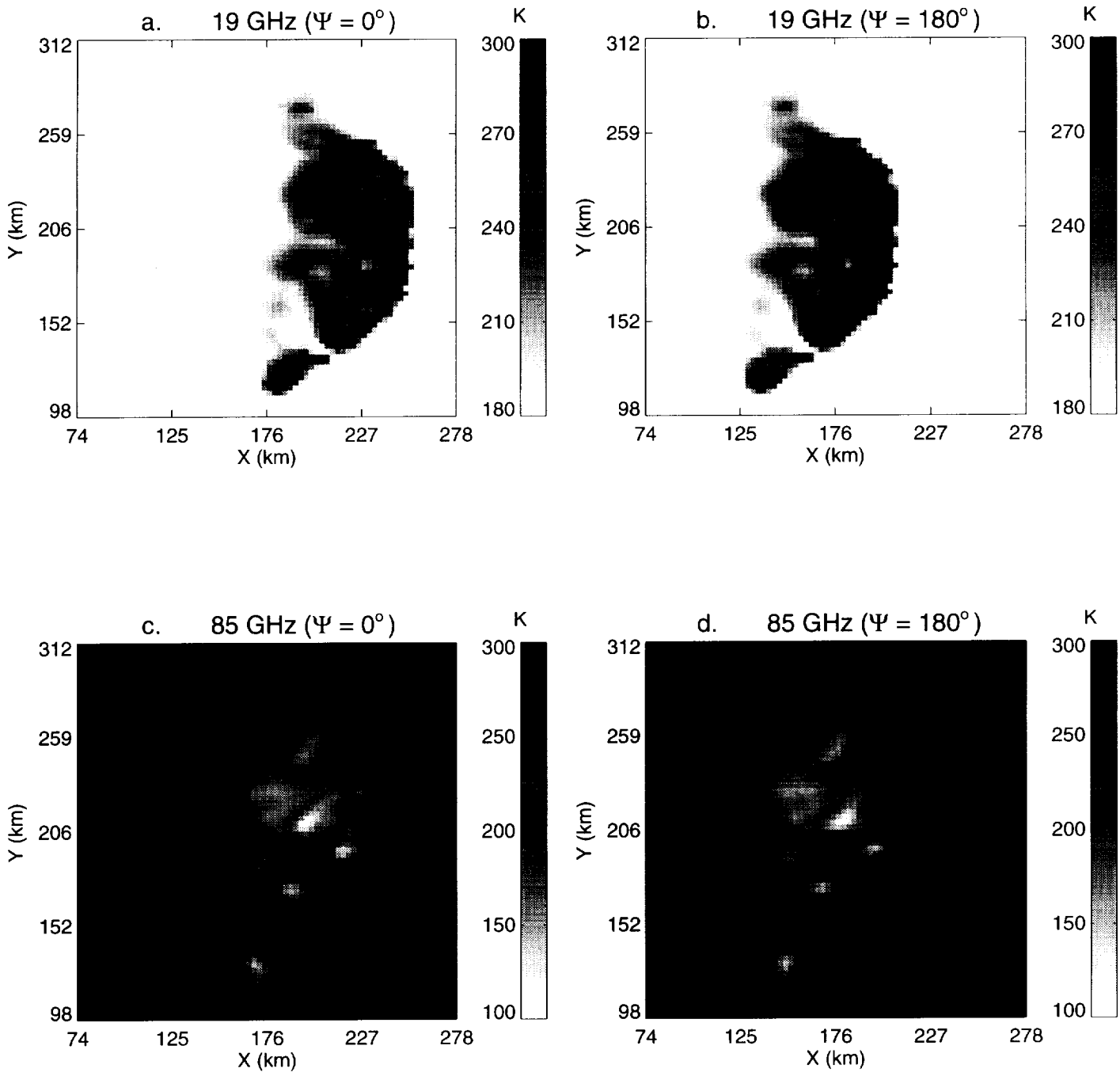
a. 19 GHz (Ψ = 0°)
b. 19 GHz (Ψ = 180°)
c. 85 GHz (Ψ = 0°)
d. 85 GHz (Ψ = 180°)
K
Y (km)
X (km)
312
259
206
152
98
74
125
176
227
278
300
270
240
210
180
250
200
150
100

Fig. 6

Fig. 7

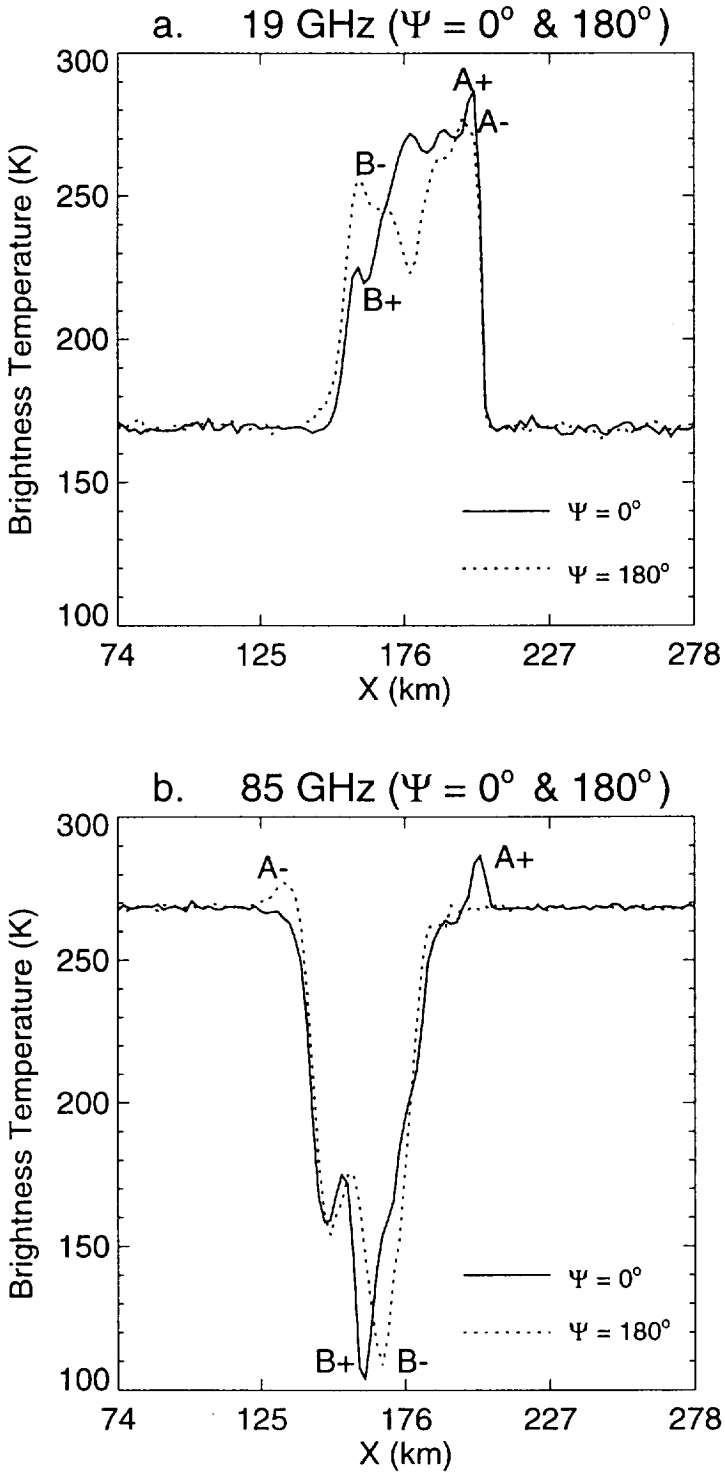
a. 19 GHz (Ψ = 0° & 180°)
Brightness Temperature (K)
300
250
200
150
100
74
125
176
227
278
X (km)
A+
A-
B-
B+
Ψ = 0°
Ψ = 180°
b. 85 GHz (Ψ = 0° & 180°)
Brightness Temperature (K)
300
250
200
150
100
74
125
176
227
278
X (km)
A-
A+
B+
B-
Ψ = 0°
Ψ = 180°

Fig. 8

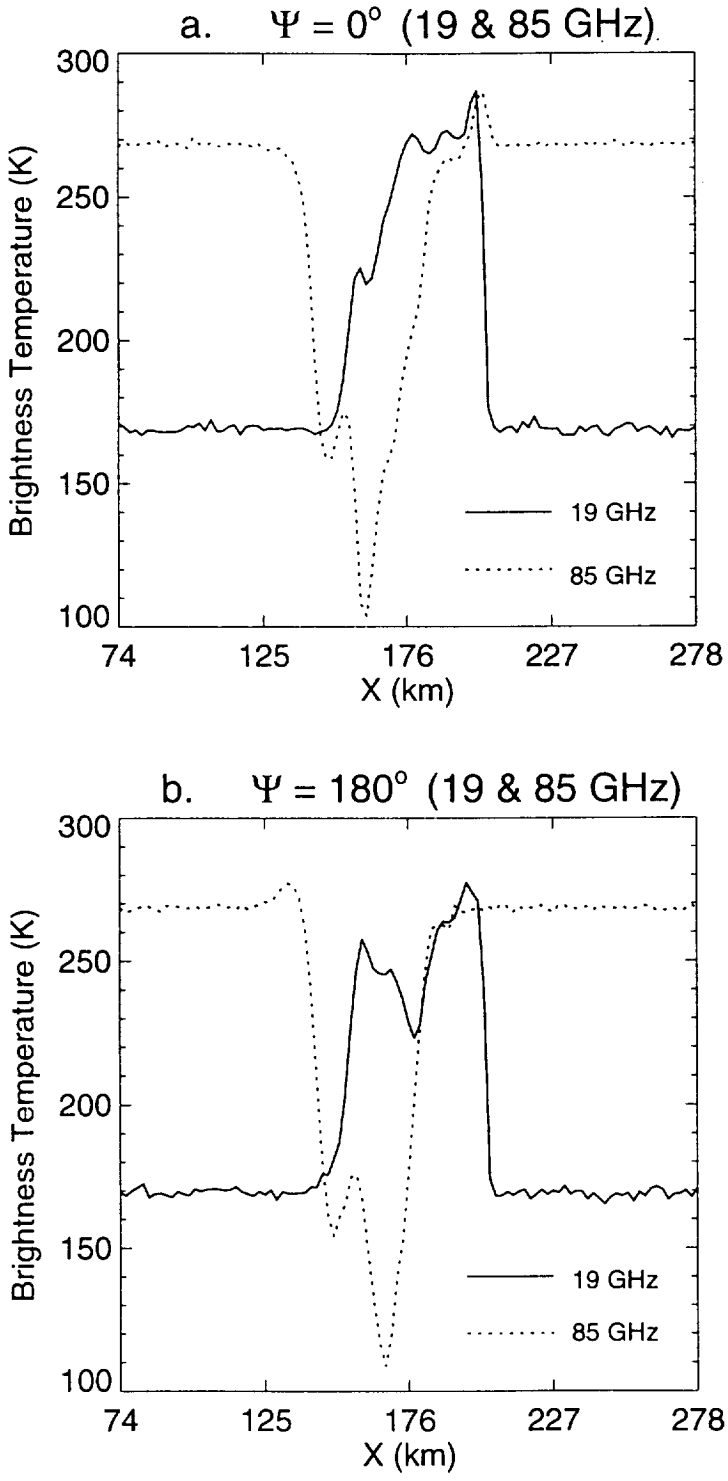
a. Ψ = 0° (19 & 85 GHz)
Brightness Temperature (K)
300
250
200
150
100
74
125
176
227
278
X (km)
19 GHz
85 GHz
b. Ψ = 180° (19 & 85 GHz)
Brightness Temperature (K)
300
250
200
150
100
74
125
176
227
278
X (km)
19 GHz
85 GHz

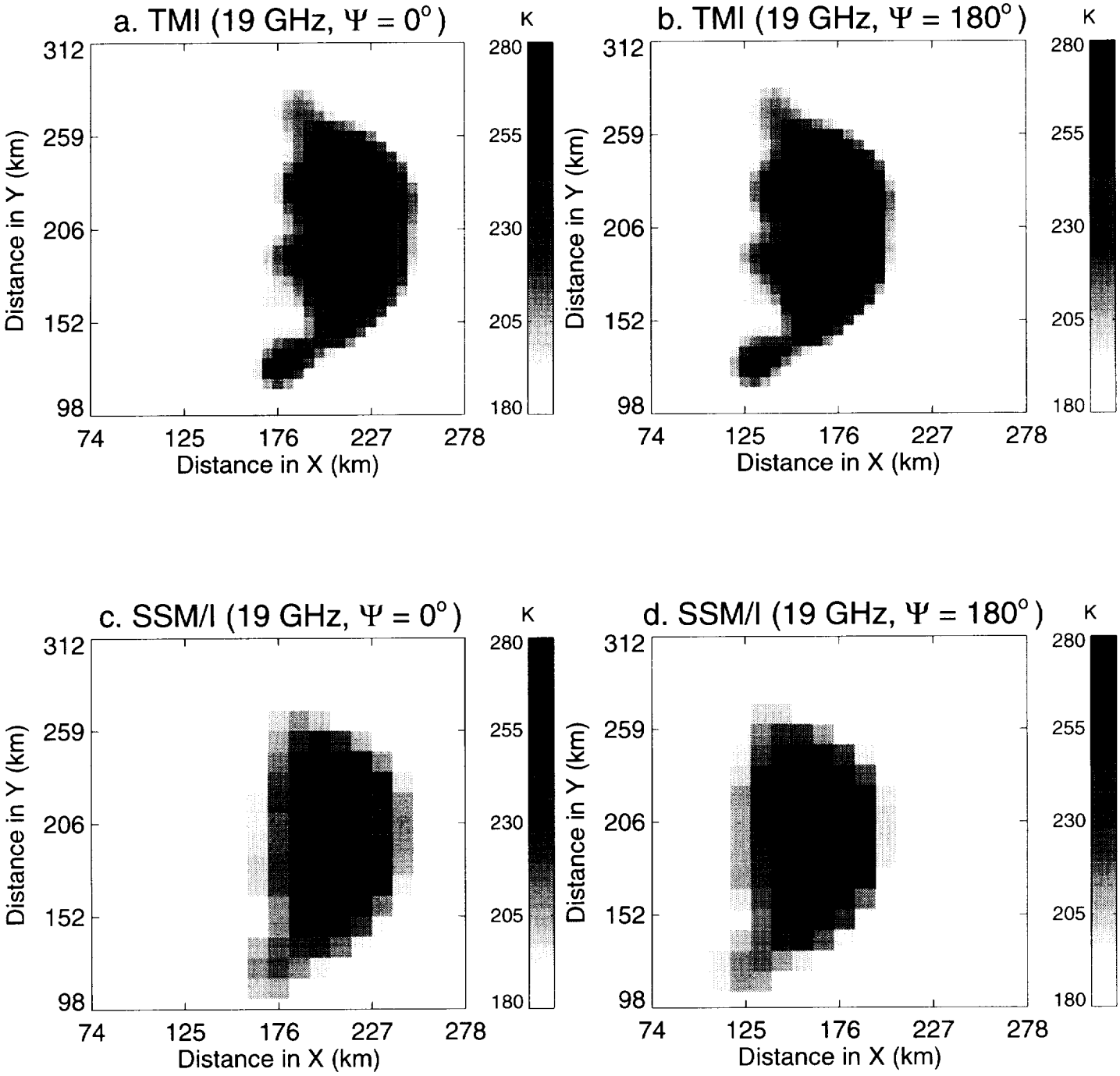
a. TMI (19 GHz, Ψ = 0°)
b. TMI (19 GHz, Ψ = 180°)
c. SSM/I (19 GHz, Ψ = 0°)
d. SSM/I (19 GHz, Ψ = 180°)
K
280
255
230
205
180
312
259
206
152
98
74
125
176
227
278
Distance in Y (km)
Distance in X (km)

Fig. 9

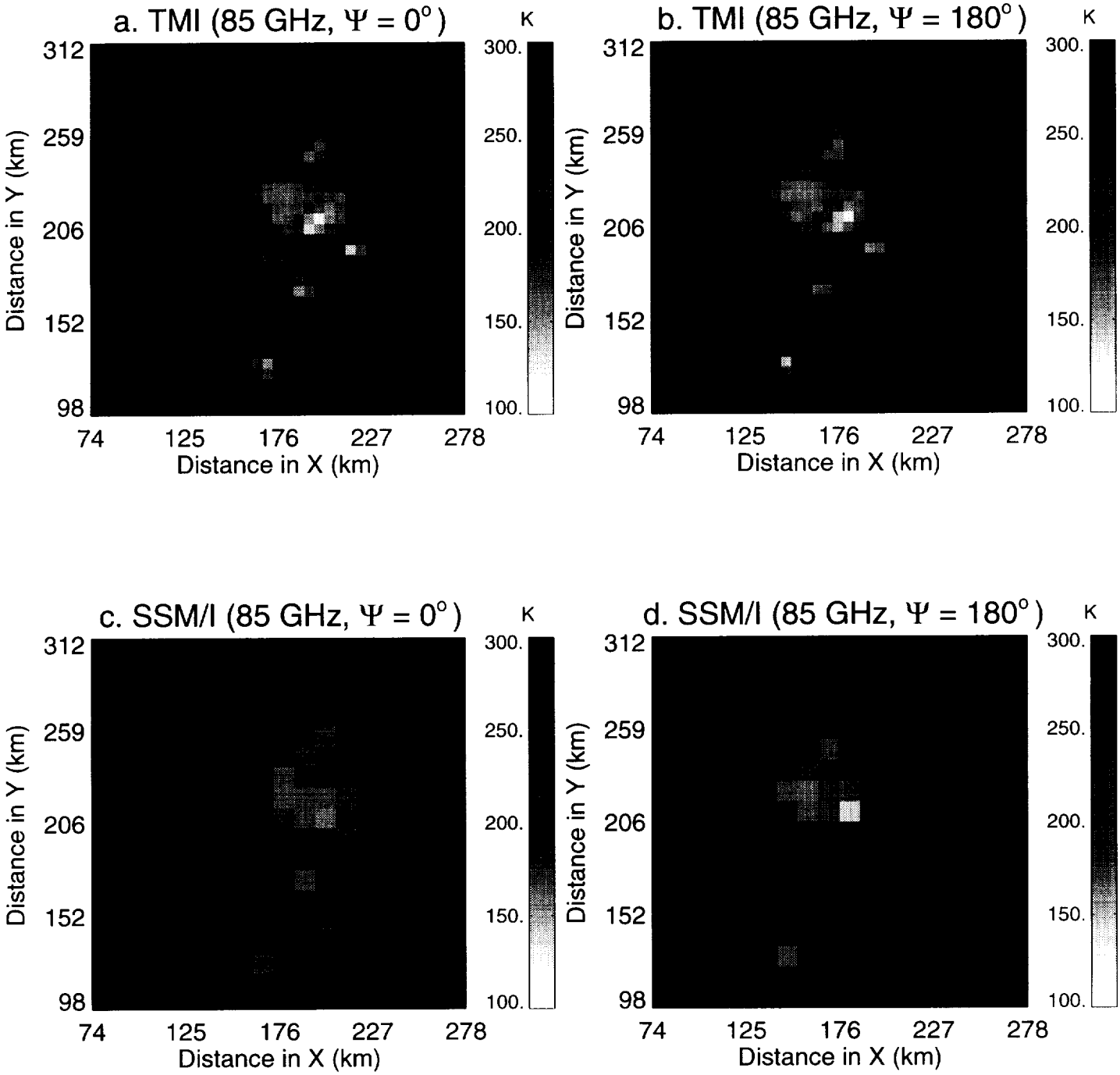
a. TMI (85 GHz, Ψ = 0°)
b. TMI (85 GHz, Ψ = 180°)
c. SSM/I (85 GHz, Ψ = 0°)
d. SSM/I (85 GHz, Ψ = 180°)
K
300.
250.
200.
150.
100.
312
259
206
152
98
Distance in Y (km)
74
125
176
227
278
Distance in X (km)

Fig. 10

Fig. 11

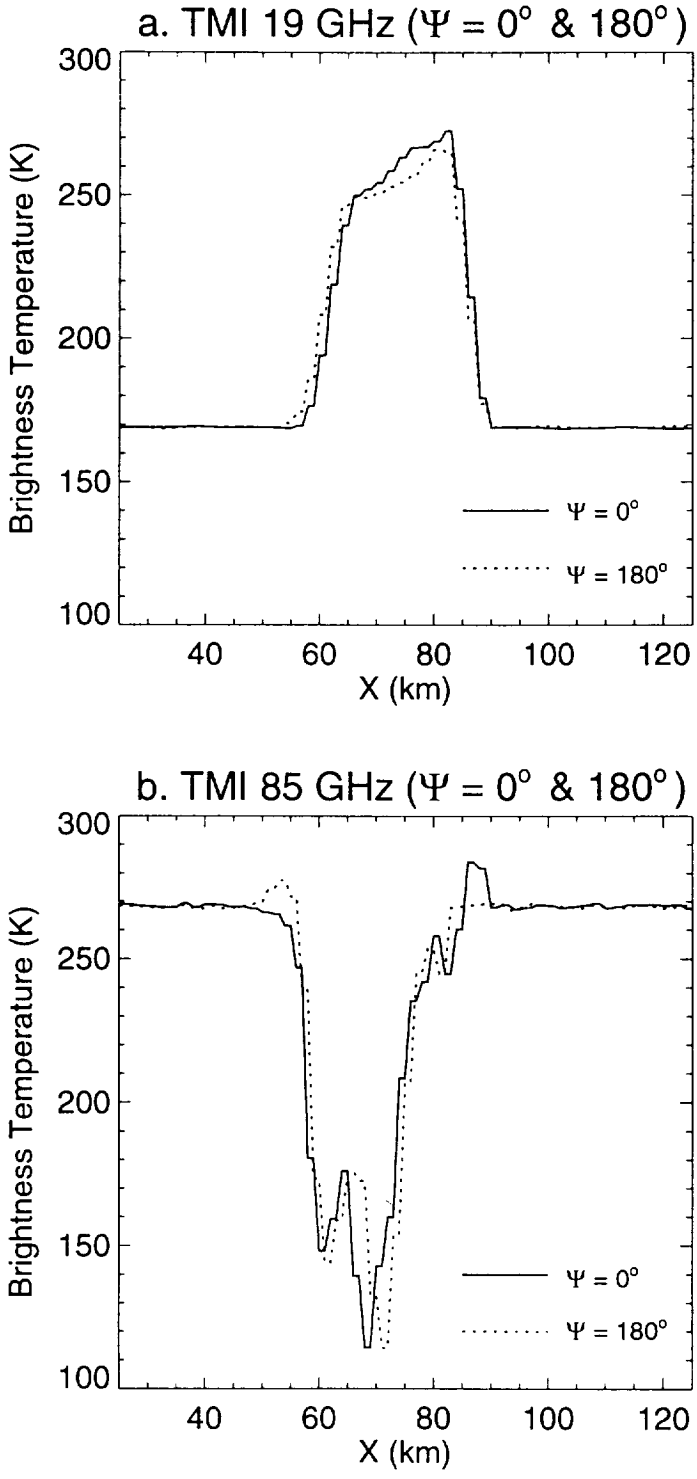
a. TMI 19 GHz (Ψ = 0° & 180°)
Brightness Temperature (K)
300
250
200
150
100
40
60
80
100
120
X (km)
Ψ = 0°
Ψ = 180°
b. TMI 85 GHz (Ψ = 0° & 180°)
Brightness Temperature (K)
300
250
200
150
100
40
60
80
100
120
X (km)
Ψ = 0°
Ψ = 180°

Fig. 12

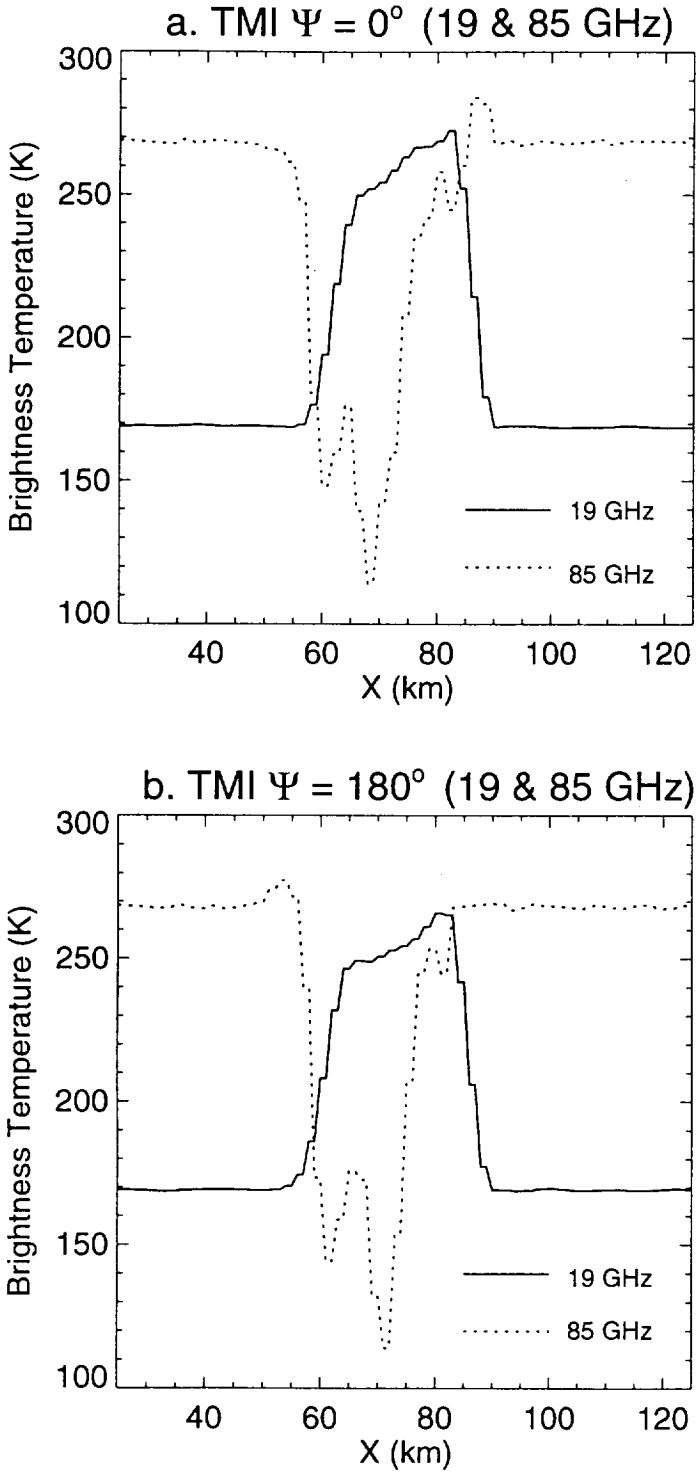
a. TMI Ψ = 0° (19 & 85 GHz)
Brightness Temperature (K)
300
250
200
150
100
40
60
80
100
120
X (km)
19 GHz
85 GHz
b. TMI Ψ = 180° (19 & 85 GHz)
Brightness Temperature (K)
300
250
200
150
100
40
60
80
100
120
X (km)
19 GHz
85 GHz

Fig. 13

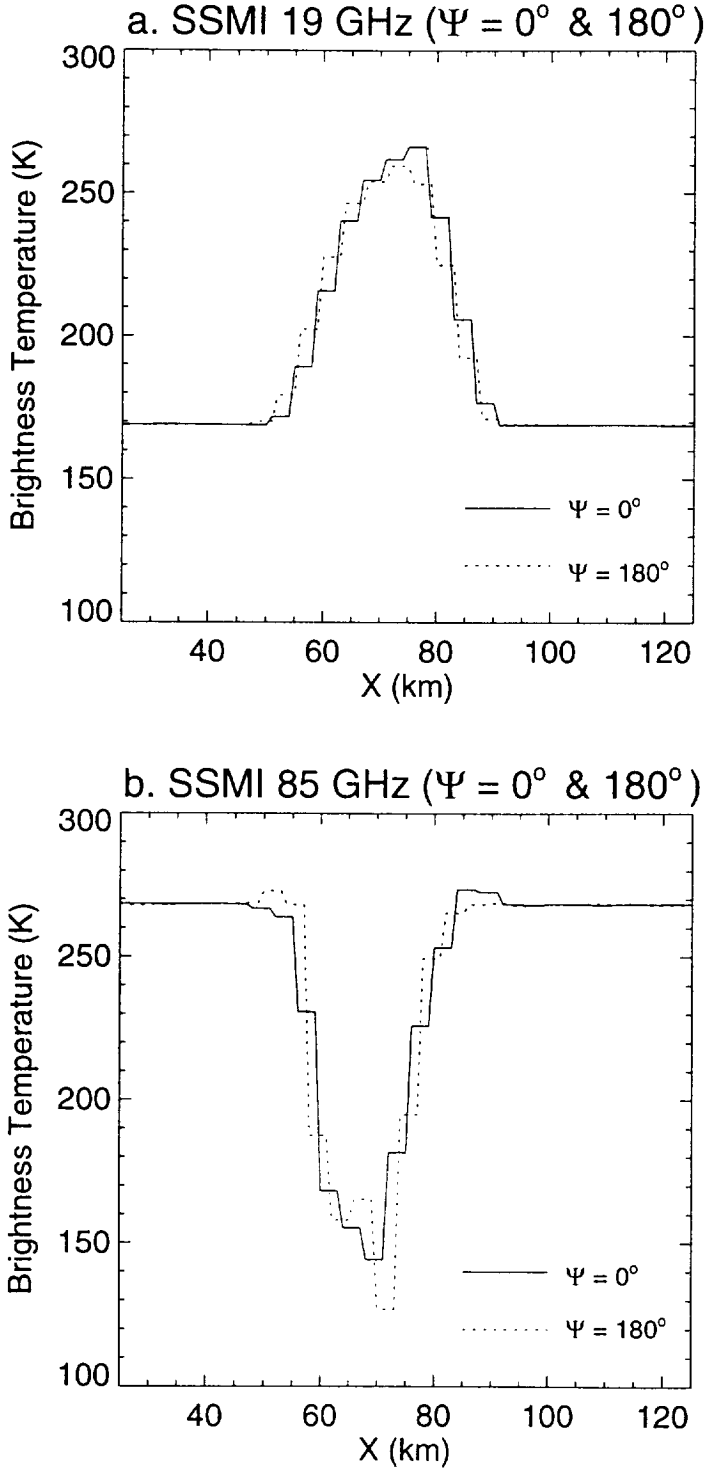
a. SSMI 19 GHz (Ψ = 0° & 180°)
Brightness Temperature (K)
300
250
200
150
100
40
60
80
100
120
X (km)
Ψ = 0°
Ψ = 180°
b. SSMI 85 GHz (Ψ = 0° & 180°)
Brightness Temperature (K)
300
250
200
150
100
40
60
80
100
120
X (km)
Ψ = 0°
Ψ = 180°

Fig. 14

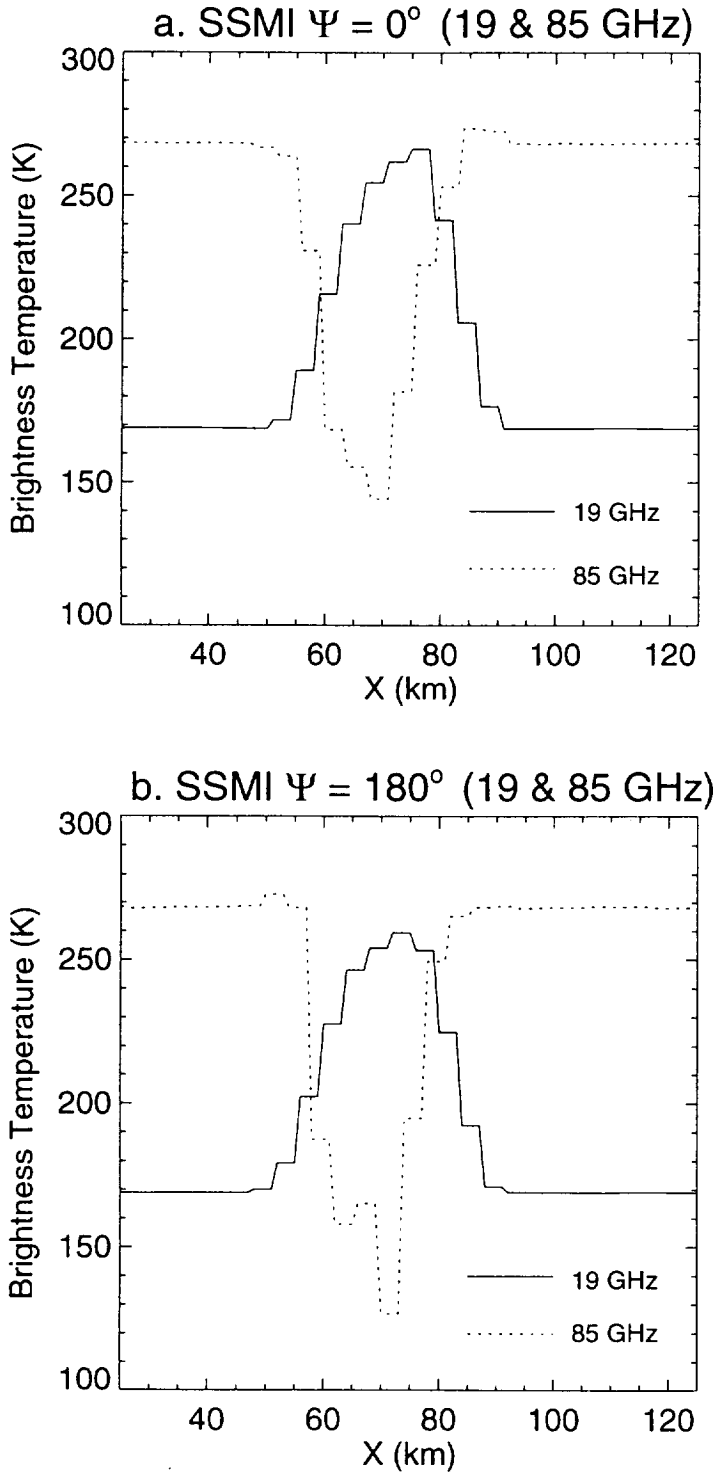
a. SSMI Ψ = 0° (19 & 85 GHz)
Brightness Temperature (K)
300
250
200
150
100
40
60
80
100
120
X (km)
19 GHz
85 GHz
b. SSMI Ψ = 180° (19 & 85 GHz)
Brightness Temperature (K)
300
250
200
150
100
40
60
80
100
120
X (km)
19 GHz
85 GHz

Fig. 15

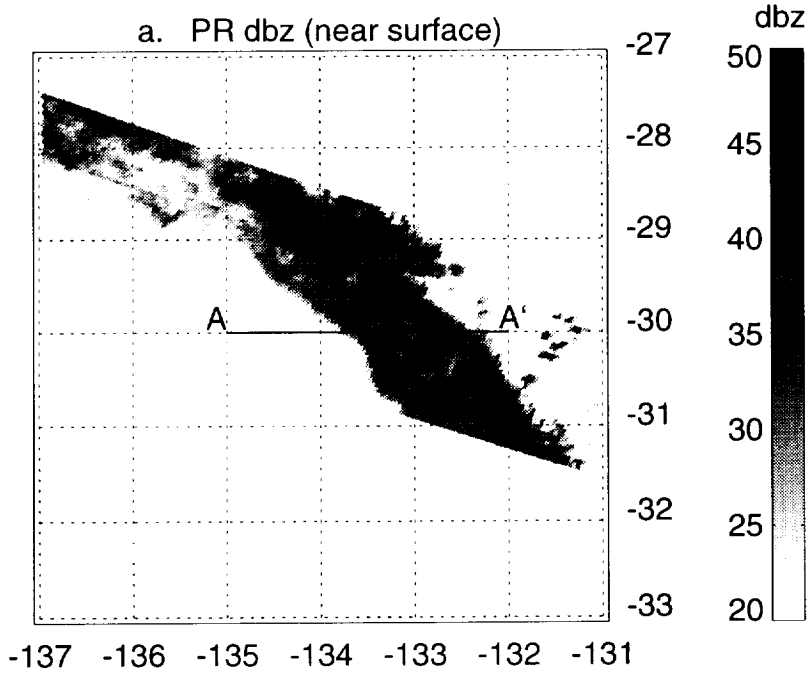
a. PR dbz (near surface)
dbz
50
45
40
35
30
25
20
A
A'
-27
-28
-29
-30
-31
-32
-33
-137
-136
-135
-134
-133
-132
-131

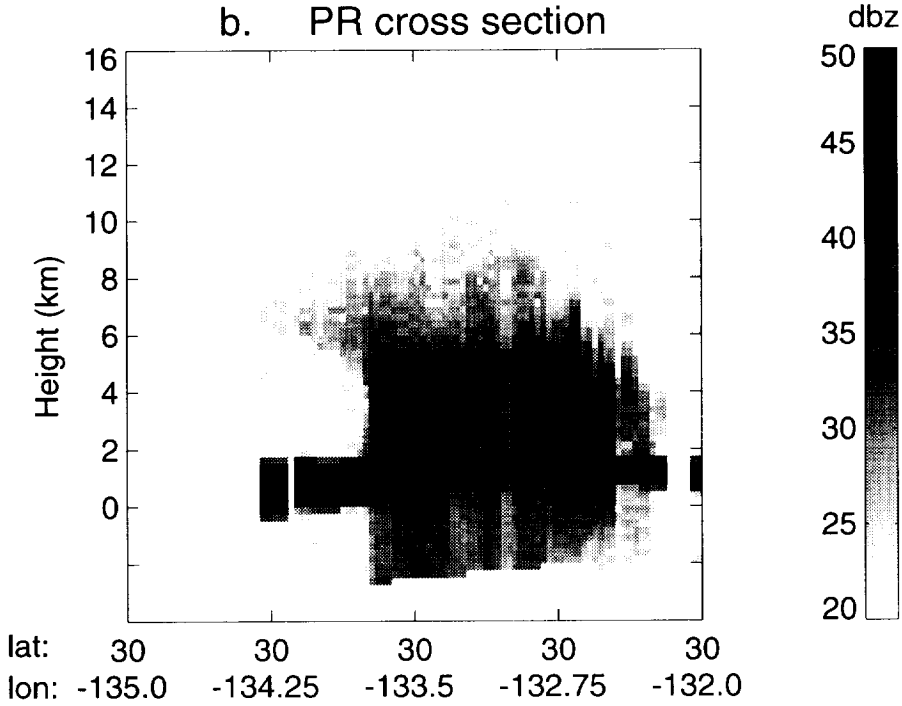
b. PR cross section
dbz
50
45
40
35
30
25
20
Height (km)
16
14
12
10
8
6
4
2
0
lat: 30 30 30 30 30
lon: -135.0 -134.25 -133.5 -132.75 -132.0

Fig. 16

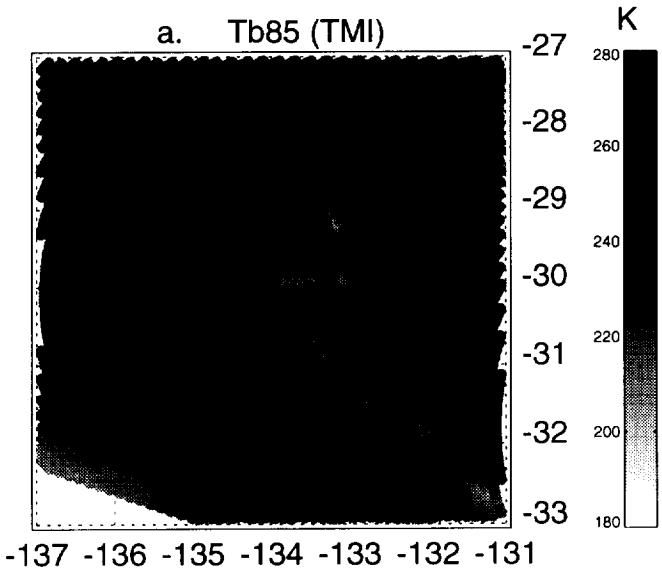
a. Tb85 (TMI)
K
280
260
240
220
200
180
-27
-28
-29
-30
-31
-32
-33
-137 -136 -135 -134 -133 -132 -131

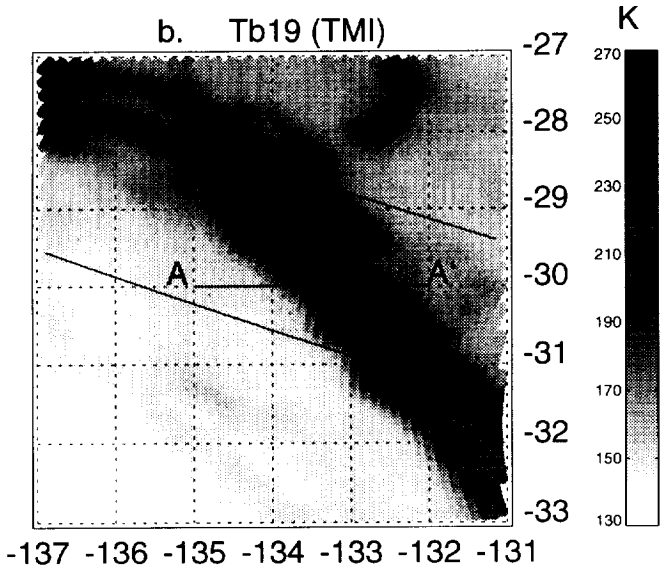
b. Tb19 (TMI)
K
270
250
230
210
190
170
150
130
A
A'
-27
-28
-29
-30
-31
-32
-33
-137 -136 -135 -134 -133 -132 -131

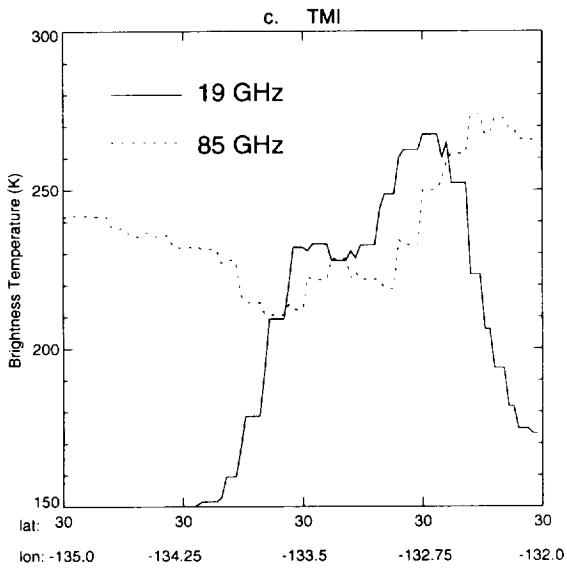
c. TMI
19 GHz
85 GHz
Brightness Temperature (K)
300
250
200
150
lat: 30 30 30 30 30
lon: -135.0 -134.25 -133.5 -132.75 -132.0

Fig. 17

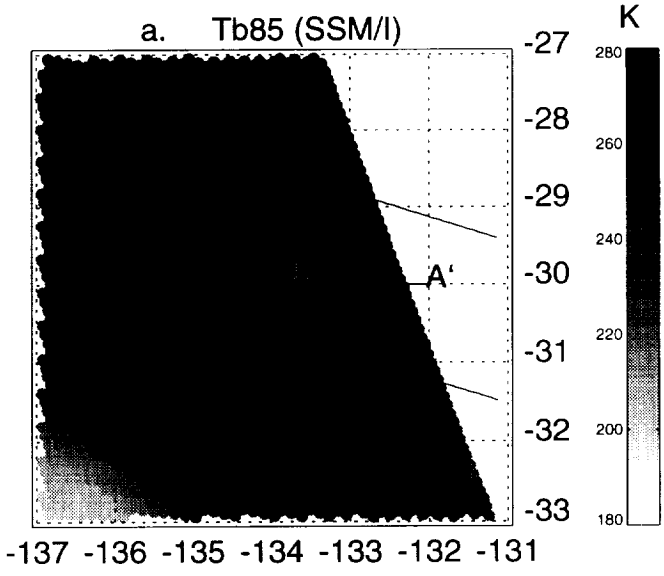
a. Tb85 (SSM/I)
K
280
260
240
220
200
180
A'
-27
-28
-29
-30
-31
-32
-33
-137 -136 -135 -134 -133 -132 -131

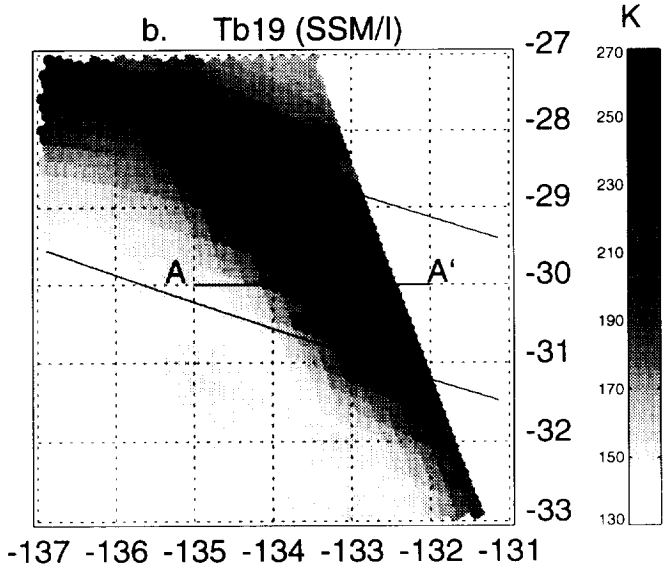
b. Tb19 (SSM/I)
K
270
250
230
210
190
170
150
130
A
A'
-27
-28
-29
-30
-31
-32
-33
-137 -136 -135 -134 -133 -132 -131

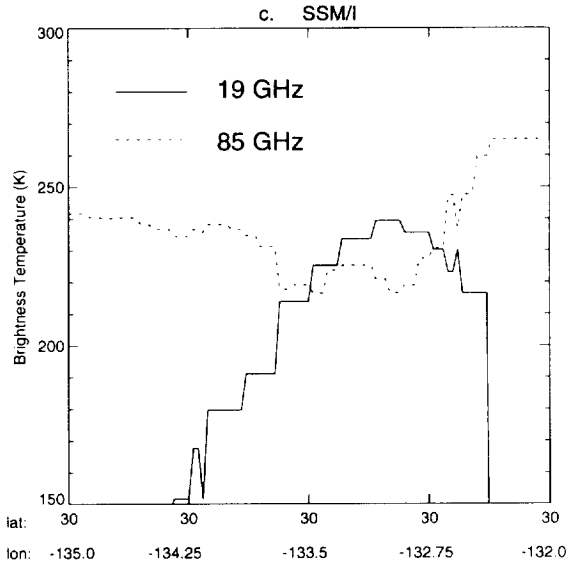
c. SSM/I
19 GHz
85 GHz
Brightness Temperature (K)
300
250
200
150
lat: 30 30 30 30 30
lon: -135.0 -134.25 -133.5 -132.75 -132.0

Fig. 18

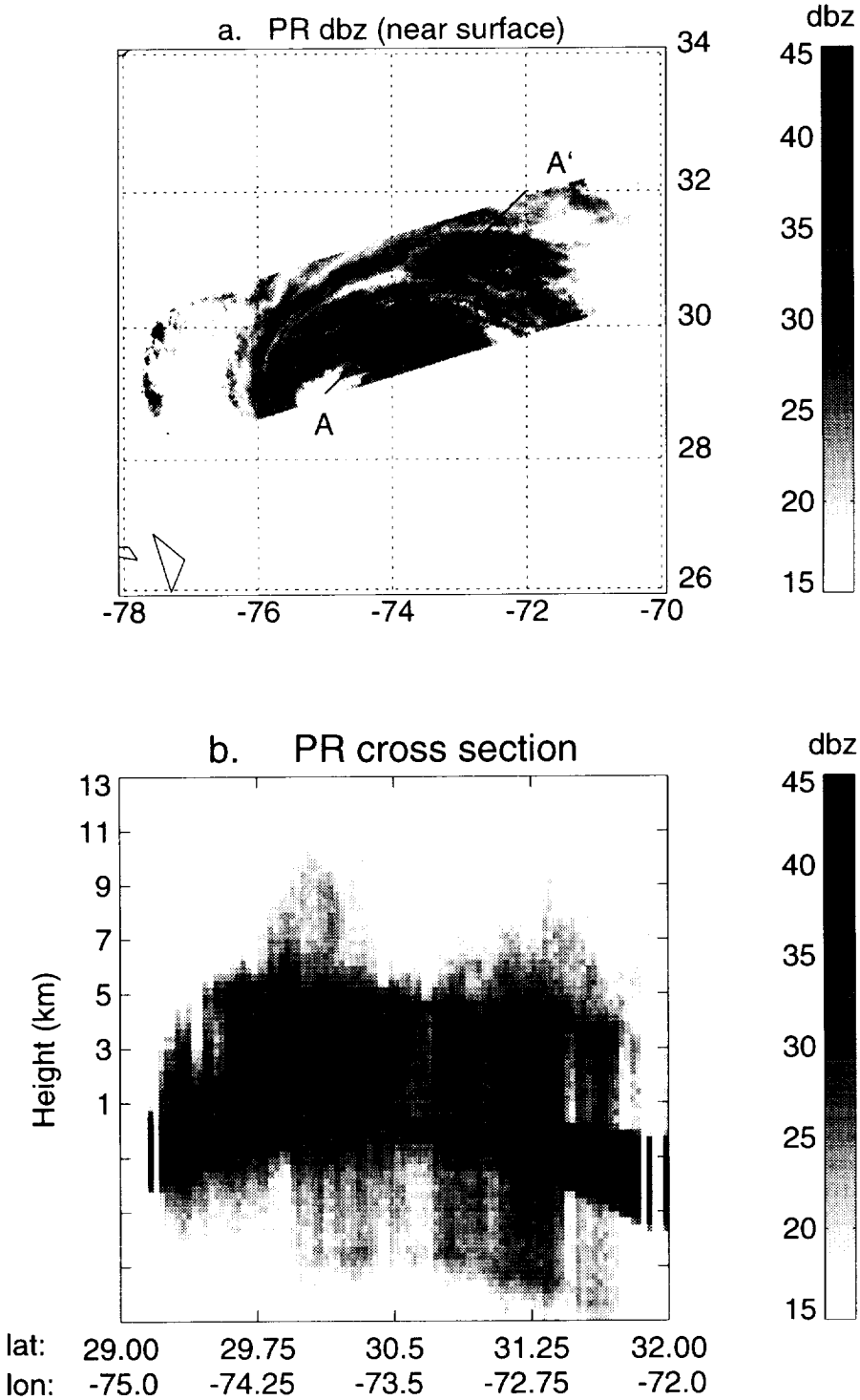
a. PR dbz (near surface)
dbz
45
40
35
30
25
20
15
34
32
30
28
26
-78
-76
-74
-72
-70
A'
A
b. PR cross section
dbz
45
40
35
30
25
20
15
Height (km)
13
11
9
7
5
3
1
lat: 29.00 29.75 30.5 31.25 32.00
lon: -75.0 -74.25 -73.5 -72.75 -72.0

Fig. 19

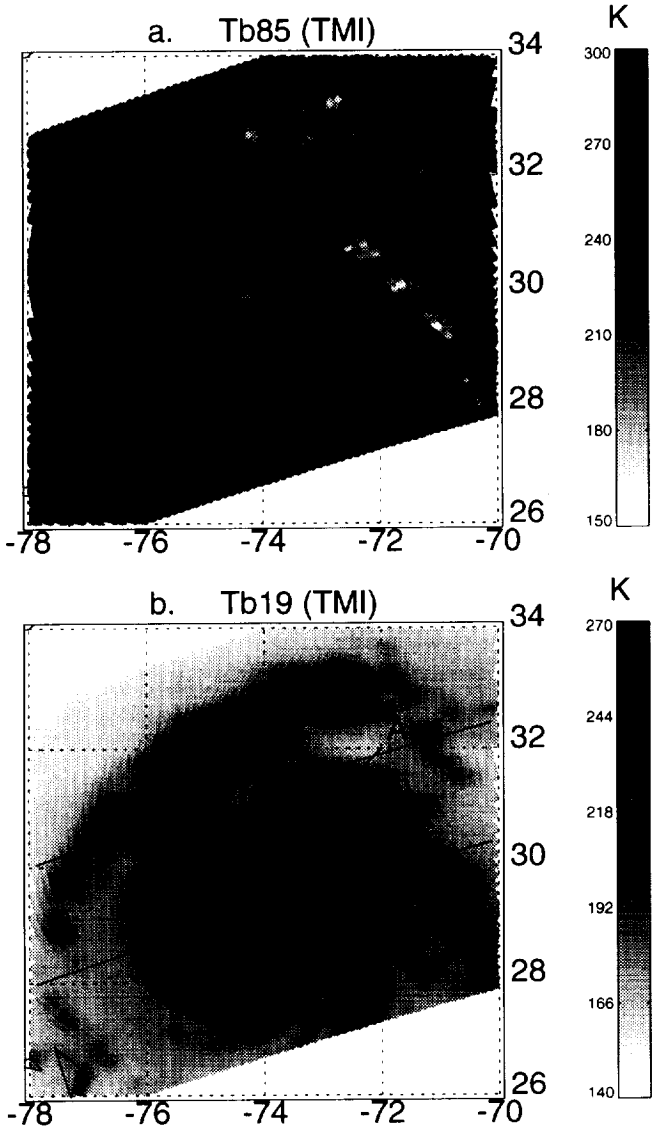
a. Tb85 (TMI)
K
300
270
240
210
180
150
34
32
30
28
26
-78
-76
-74
-72
-70
b. Tb19 (TMI)
K
270
244
218
192
166
140
34
32
30
28
26
-78
-76
-74
-72
-70
c. TMI
Brightness Temperature (K)
300
250
200
150
19 GHz
85 GHz
lat: 29.00
29.75
30.5
31.25
32.00
lon: -75.0
-74.25
-73.5
-72.75
-72.0

Fig. 20

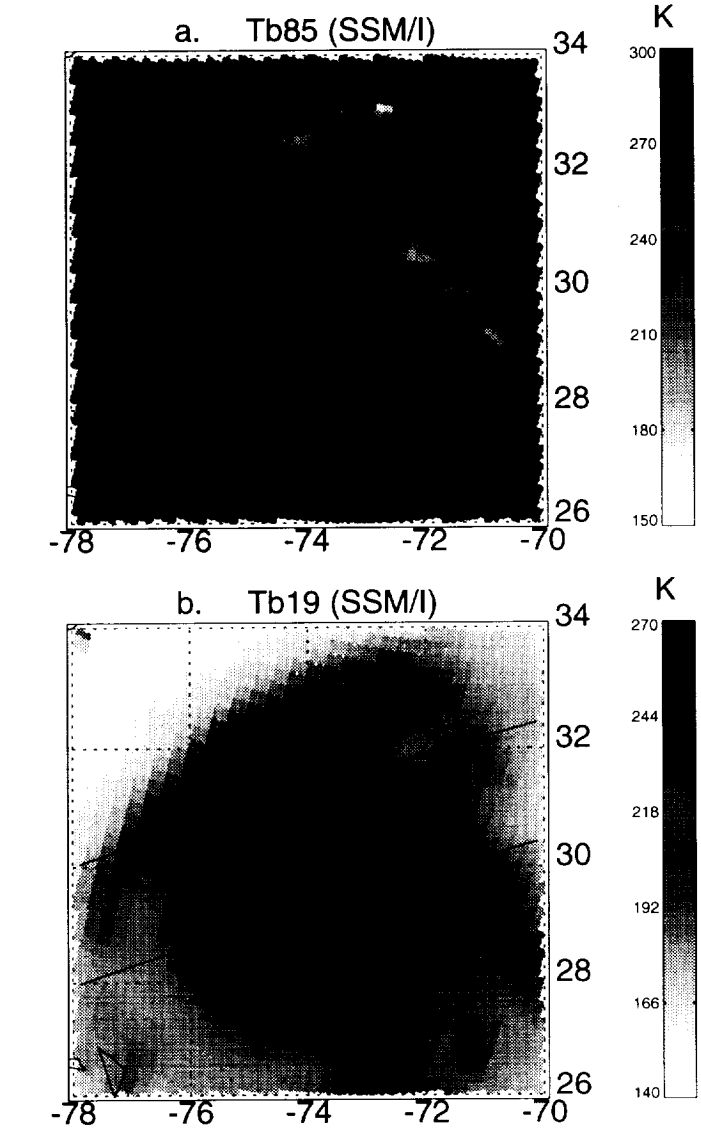
a. Tb85 (SSM/I)
K
300
270
240
210
180
150
34
32
30
28
26
-78
-76
-74
-72
-70
b. Tb19 (SSM/I)
K
270
244
218
192
166
140
34
32
30
28
26
-78
-76
-74
-72
-70
c. SSM/I
Brightness Temperature (K)
300
250
200
150
19 GHz
85 GHz
lat: 29.00
29.75
30.5
31.25
32.00
lon: -75.0
-74.25
-73.5
-72.75
-72.0